Helium Bubbling in the Molten Salt Fast Reactor

Optimisation of measurement methods and reasearch on extraction methods in a flotation column

Anne Grooten

A thesis presented for the degree of Bachelor of Science

Student number:	5125154
Project duration:	August 28, 2021 – November 10, 2021
Defence date:	29 November 2021, 13:30
Thesis committee:	Dr. ir. M. Rohde, TU Delft, supervisor
	T. Dumaire, TU Delft
	Dr. A. Smith, TU Delft

Transport Phenomena in Nuclear Applications
Delft University of Technology
The Netherlands

Acknowledgements

In the experiments and the writing of this Bachelor's Thesis, I have been greatly helped by the following people. Firstly, Ies Lakerveld, on whose work this has been a continuation, and whose thesis has greatly inspired the theoretical and methodological chapters of my thesis. John Vlieland and Dick de Haas were always able to help and think along whenever I encountered a problem. Martin Rohde was my supervisor during this project and always asked the questions which got me thinking again if I got stuck, provided a knowledgeable but distant opinion on the work I did, seeing the broader view when I was mainly focussed on the details. Special thanks goes to Thomas Dumaire, who taught me how to work with the setup and the DaVis software, prepared particle samples, provided useful insights on the measurements I was doing, and generally was the person I would discuss the details of my project with.

Abstract

With world-wide energy demands ever increasing and global warming posing ever greater problems to human habitation on Earth, new, renewable energy sources are in great demand. Often excluded from this list of gashouse-emission free energy sources is nuclear energy. Nuclear energy is generated from the fission reaction of fissile materials, most commonly Uranium-235. To expand the range of materials usable for nuclear fission, the SAMOSAFER (Severe Accident MOdelling and Safety Assesment for Fluid-fuel Energy Reactors) project is working on the development of a Generation-IV reactor called the Molten Salt Fast Reactor (MSFR). The project is connected to a great many universities, research groups, institutions and companies world-wide. The great objective is to have the MSFR operational by 2050.

In this research, the aim is to investigate one aspect of the MSFR, namely the removal of solid reaction products from the fuel salt, to avoid the poisoning of the reaction and corrosion of the reactor core. The removal of the noble metal nanoparticles and gaseous fission products is done through helium bubbling. In this research, a simulant fluid with similar viscosity to the fuel salt and fluorescent nanoparticles will be used to measure the particle extraction rate in a bubble column using three different extraction methods. The measurements are done using the Laser Induced Fluorescence (LIF) technique, where a laser is formed into a sheet, which illuminates a single layer of the bubble column. The fluorescent particles in this layer absorp the laser light and emit another wavelength, which is then led through a selective filter to a time-gated camera and formed into an image. The images are processed and calibrated to determine the particle concentration before, during and after bubbling.

The results show that none of the three used extraction methods, the evaporation of particles at the fluid-air interface, the use of a Hallimond tube and the use of filter paper, is effective in neither water nor the simulant aqueous glycerol as no significant decrease in particle concentration could be found. However, it was found that it is possible to correct images taken while bubbling for the reflections of fluorescent light, which enables the comparison between images taken while bubbling and images taken while the fluid is at rest.

Contents

1

Introduction to the experiment

The introductory chapter of this report is divided into three parts. First, some background information about nuclear energy is given in Chapter . Secondly, in Chapter the operation of the reactor under investigation is explained. Lastly, Chapter concludes the introduction by discussing the specific topic of this research, helium bubbling.

1.1. Nuclear energy

The first nuclear reactor was built only 4 years after the discovery of nuclear fission by Otto Hahn in 1938. In December 1942, Enrico Fermi and his team initiated the first self-sustaining nuclear chain reaction made by humans in what he himself described as "a crude pile of black bricks and wooden timbers"[1]. Since then, much research has been done to promote efficiency and safety of nuclear reactors. This section will discuss the physics of nuclear energy and its environmental impact.

1.1.1. Nuclear physics

The starting point of the most commonly used nuclear fission is an isotope of uranium, U-235. Its fission reaction is as follows:

$$^{235}\mathrm{U} + \mathrm{n} \rightarrow \mathrm{X}+\mathrm{Y} + \nu\mathrm{n} \tag{1.1}$$

Reaction products X and Y emerge from the reaction with high kinetic energy E_k, which is transformed into heat as the reaction products are slowed down by colliding with other particles in the reactor fuel [2]. The high-energy neutrons that emerge from the reaction should be sufficient to sustain the chain reaction, however, not every neutron causes a new fission, which makes it difficult to keep a stable chain reaction going.

The natural sources of uranium contain mostly non-fissile uranium-238. Less than 1 % of the world's uranium is the fissile uranium-235. Uranium only becomes a good nuclear fuel if it has around 3-5% uranium-235. The uranium therefore needs to be enriched to increase the percentage of U-235[3]. For fissile products, the higher the energy of a neutron, the lower the probability that a fission reaction will take place. Therefore, reactors use a moderator to slow down the neutrons and increase heat production[4]. These slowed-down neutrons are called thermal neutrons.

1.1.2. Environmental impact

Even though its environmental impact is low compared to fossil fuels, nuclear power is usually not listed as an environmentally friendly energy source. The accidents in the reactors at Chernobyl in 1989 and at Fukushima in 2011 have raised strong public opinions against nuclear power regarding population health and surrounding environment[5]. The safe storage of radioactive waste is a concern, as well as the mining of the fuel source. The mining of uranium is not environmentally friendly, with open-pit mining leaving radioactive waste scattered around the mining site and underground mining exposing mine workers to high levels of radiation[6]. Additionally, the building costs of a reactor are high and nuclear power is a long-term investment.

Even though there are many concerns, nuclear energy has low carbon emission (usually in the range of 6–10 g CO_2/KWh[7], which is 45 times less than coal[8]). It also requires less land to operate than other clean energy

sources, as wind farms require 360 times more land area to produce the same amount of electricity and solar photovoltaic plants require 75 times more[9]. Furthermore, the resources that are accessible with current mining are sufficient for reactors to run more than 100 years at current rates of consumption [10]. To summarise: nuclear power can be an attractive long-term investment if current obstacles can be overcome.

1.2. Molten Salt Reactor

The Molten Salt Reactor (MSR) was first proposed in the 1960's and is a thorium based breeding reactor where the fuel is dissolved in the fluoride salt moderator. Chapter 1.2.1 will shortly discuss the history of the molten salt reactors, and chapter 1.2.2 will discuss the Molten Salt Fast Reactor, which is the reactor currently under development.

1.2.1. History of Molten Salt Reactors

Construction of the first molten salt reactor, called the Molten Salt Reactor Experiment (MSRE) was started in 1962 at Oak Ridge National Laboratory, and worked until 1969. The MSRE had a thermal power of 8 MW and operated either with U-233, U-235 or Pu-239. However, the fuel salt did not contain any thorium. The experience that was gained during the MSRE was used to design the Molten Salt Breeder Reactor (MSBR). The MSBR had a large core to reduce neutron leakage and a low power density to reduce irradiation damage to the graphite moderator. However, the MSBR was never built [11].

1.2.2. The Molten Salt Fast Reactor

The Molten Salt Fast Reactor is the Gen-IV reactor this research pertains to. It is part of the SAMOSAFER(Severe Accident MOdeling and Safety Assessment for Fluid-fuel Energy Reactors) project of the European Union research and innovation programme Horizon 2020. The project started October 1, 2019 and is connected to many universities, institutions and companies all over the world, including the Nuclear Research and consultancy Group (NRG) and the Delft University of Technology (TUD). The grand objective is to ensure that the MSR can comply with all expected regulations in 30 years.

The main difference between the MSRE reactor and the MSFR developed by SAMOSAFER is that the MSFR has a single salt mixture acting both as a fuel and as a coolant. By using a graphite moderator neutrons will be slowed down to be thermal, while otherwise a fast neutron spectrum would result[11].

Figure 1.1 gives an overview of the MSFR. The fission reaction takes place in the "Primary Fuel Circuit", which contains the reactor core including the blanket, primary pumps, and heat exchangers for power production. The "Emergency Drain System" is where the fuel salt will be stored in case the reactor overheats or in case of manual interruption. The fission chain reaction will then be stopped. The "Fuel Treatment Unit" is where fission products will be removed from the fuel salt and to keep the Redox potential of the salt in the right range to reduce corrosion. The heat from the reactor is transported to a turbine in the "Energy Conversion System" which drives a generator to produce electrical energy[11].

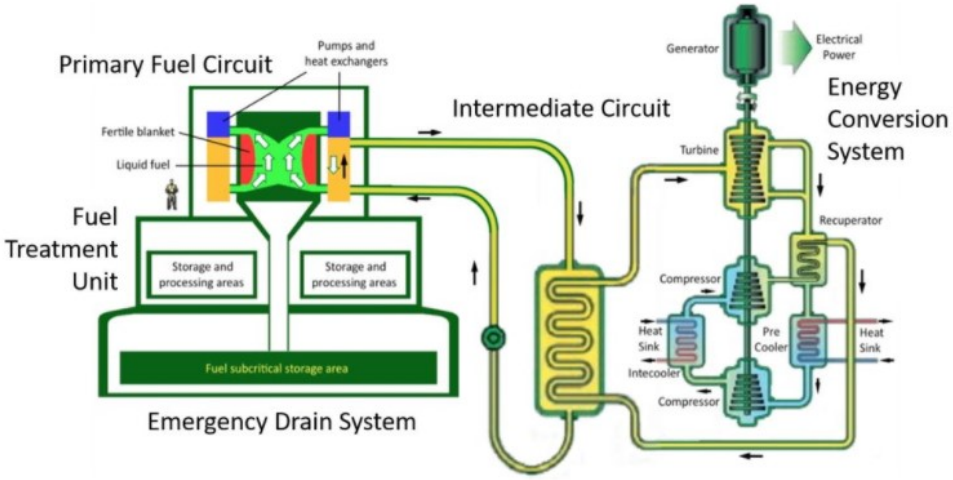

Figure 1.1: Overview of the Molten Salt Fast Reactor[11]

The fission reaction products formed in the MSFR need to be removed in order to avoid processes like corrosion of the reactor core. The elements formed in the MSFR are shown in figure 1.2. The yellow elements form fluorides and remain dissolved in the fuel salt. The elements shown in blue are gaseous fission products (GFP's). The purple elements are noble metals, which need to be removed from the fuel salt before they deposit on the cold parts of the PFC (e.g. on the heat exchanger) to prevent corrosion. The GFP's can be removed by helium bubbling, and the aim of this research is to see whether helium bubbling can also remove the noble metal particles of sub-micron size.

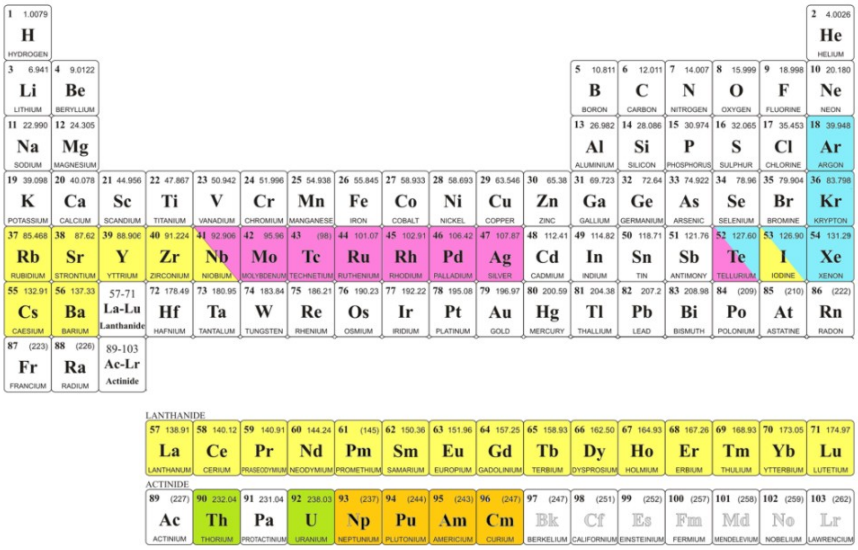

Figure 1.2: Overview of the elements formed in the fuel salt. Yellow elements remain dissolved in the fuel salt. The noble metals (purple) and GFPs (blue) removed from the fuel salt via helium bubbling and/or fluorination [11].

1.3. Aim of the research

Research into removal of micron-scale particles has been conducted by Capelli as part of her Post-Doc. She used molybdenum and iron particles to study the removal of micron-sized particles by bubbling [12]. Rozing planned on continuing and extending her work for his master's thesis, but due to the outbreak of Covid-19 in the spring of 2020, he had to fall back on off-campus research. He used a two phase Euler method to model the helium bubbling process in OpenFOAM, an open-source computational fluid dynamics program [13]. The on-campus research that was planned by Rozing was in the end carried out by Lakerveld, who worked on the removal of sub-micron particles by bubbling. Lakerveld set up the working process and did research into the behaviour of the polystyrene nanoparticles in a bubble column, as well as researching the effectivity of the Hallimond tube [14].

This Bachelor's Thesis has continued and extended the research done by Lakerveld, while working on the same setup. It uses fluorescent nanoparticles to simulate the behaviour shown by nano-sized solid fission products in the MSFR and tried o extract them from the bubble column. The experimental part of this research has taken place at the Reactor Institute Delft (RID), details regarding the experimental setup will be discussed in chapter 3. The results of the research will also be used by NRG to test numerical methods.

The main research questions that I will try to answer during this thesis are:

- How can the measurement method be optimised?
- What are efficient methods for particle collection in the top of the bubble column?

The first question arises from the discussion of the results of Lakerveld, who encountered several unexplained results. Investigated are the temperature of the column in time while bubbling, the effect of bubbling on the measured particle concentration and the accuracy of the gas flow rate. The results of these measurements can be found in chapter 4.

A number of parameters make it difficult to answer the second question, the temperature, pressure, particle/bubble size and velocity, density, viscosity, contact angle, surface tension, hydrophobicity, gas holdup, column

geometry and possibly more may all contribute to the particle extraction efficiency [13]. It is important to separate the material properties from the flow properties. The gas flow rate may also play a large role, as it determines the flow regime, and each regime has different processes that govern the particle extraction. The type of simulant fluid is of interest because an experimental setup including the fuel salt composition in the MSFR that operates at temperature T = 900 K is not available. The measurements are done using both water and a water-glycerol solution, which is a suitable substitute for the fuel salt [13] [12]. Three different types of particle extraction methods are investigated on the aspect of particle extraction efficiency. The results of the extraction measurements can be found in chapter 4.

2

Theory

To properly understand and conduct experiments on particle flotation, a thorough understanding of underlying physical processes is required. The purpose of this chapter is to get a better understanding of the context in which the research is conducted and which factors are of significance. Section 2.1 discusses the modelling of multiphase flows, section 2.2 goes into detail about the bubble-particle attachment model, and section 2.4 describes the difference in the behaviour of nanoparticles to micron-sized particles.

2.1. Multiphase flows

Gas bubbles in a liquid can transport from 20 up to 50 times more particles than an average suspension of just particles in a liquid [15]. The adhesion of particles to the bubble surface enables the bubbles to transport particles in the direction of the bubble flow. However, as three different phases are present, the flow becomes quite difficult to model. Two methods for determining the flow regime and the influence of important parameters are given in this section.

One way to define different flow patterns is by Reynolds number, given by the ratio of inertial forces to viscous forces within a fluid. It helps predict flow patterns in different fluid flow situations. The bubble Reynolds number Re_b is defined in equation 2.1:

$$Re_b = \frac{\rho_l v_b d_b}{\mu}, \tag{2.1}$$

where ρ_l is the fluid density, v_b is the bubble rising velocity, d_b is the bubble diameter and μ is the fluid viscosity. With the help of Re_b, three regimes can be discerned:

$$\begin{cases} Re_b \ll 1 & \text{Stokes flow} \\ 0.2 < Re_b < 100 & \text{Intermediate flow} \\ Re_b > 100 & \text{Potential flow} \end{cases} \tag{2.2}$$

Typical bubble Reynolds numbers encountered for the sizes of bubbles employed during flotation fall in the intermediate flow regime [16], which places certain bounds on the fluid viscosity.

Another way to define flow characteristics is by looking at the flow pattern. This indicates the visible distribution or structure between the gas and the liquid. Figure 2.1 shows the different flow patterns as a function of the gas velocity v_{sg} and the liquid velocity v_{sl} in a vertical column. Figure 2.1 also shows visually the different flow patterns. The desired flow pattern is bubbly flow, which occurs at low gas velocities where very small bubbles rise in rectilinear motion. Larger bubbles rise on randomized trajectories and may form even larger bubbles [17]. The formation of larger bubbles results in a relatively smaller total surface area compared to smaller bubbles so that particles have a lower probability of interacting with the bubbles, and therefore a lower collection efficiency [14].

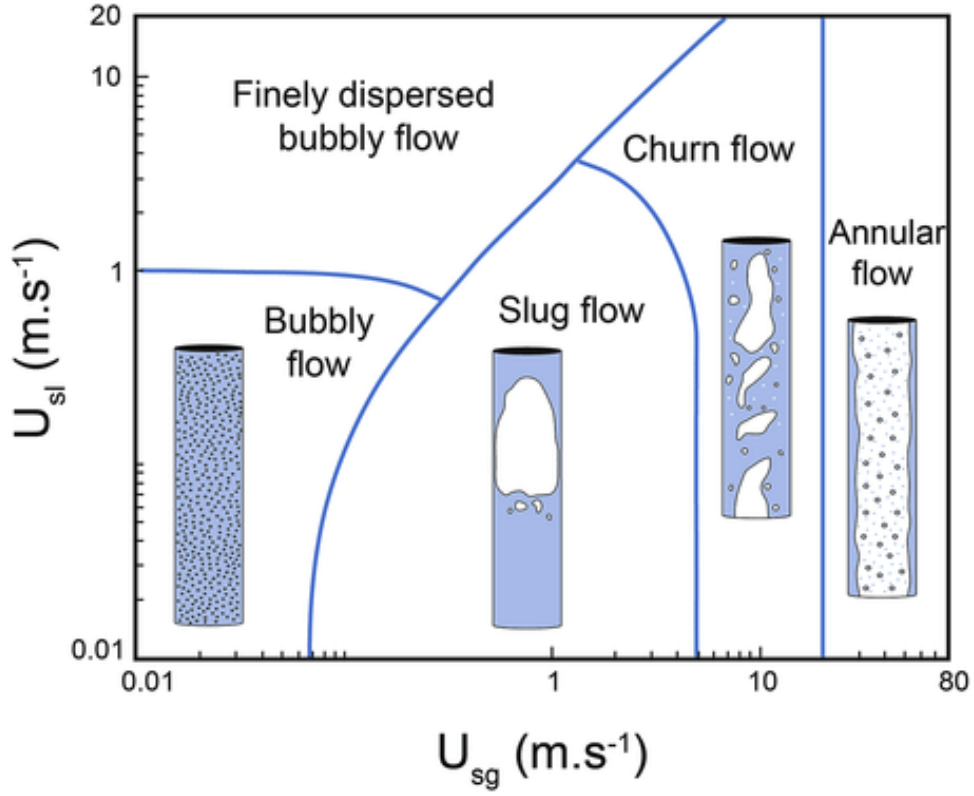

Figure 2.1: Flow pattern map for a 72-mm inner diameter vertical pipe flow of air and water according to the model of Taitel et al. (1980) [18].

2.1.1. Temperature and viscosity

As discussed above, the viscosity of the fluid can greatly influence the behaviour of the gas bubbles. The viscosity of a fluid can be influenced by the temperature of the fluid. Generally: the higher the temperature of the fluid, the lower the viscosity. There can be found several relations for viscosity and temperature, but they are only applicable in specific cases and temperature ranges [19] and shall not be discussed here.

2.2. Bubble-particle interactions

The central process in froth flotation is the capture of particles by rising bubbles [20]. This capture, the collection efficiency, is defined as:

$$E = E_c E_a E_s, \tag{2.3}$$

where E_c is the collision efficiency, E_a is the attachment efficiency and E_s is the stability efficiency of the bubble–particle system. This division of the collision efficiency was proposed by Derjaguin and Dukhin [21], and divides the collision process where, in order, hydrodynamic interactions, interfacial forces and bubble–particle system stability dominate. These zones are not discrete, rather, they grade into one another. The divistion of the different zones is illustrated in figure 2.2.

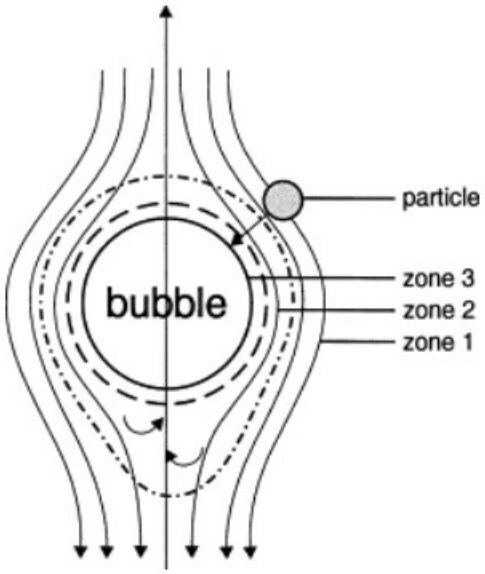

Figure 2.2: Hydrodynamic (1), interceptive (2) and surface force (3) zones of interaction between a bubble and a particle [21]. The first two zones are the zones where the collision process takes place, whereas in the third zone, the attachment of particle to bubble occurs.

In the first zone, the hydrodynamic forces are dominant. The drag force on the bubble forces the particle to follow the streamlines around the bubble. The larger the viscosity of the fluid and thus the more resistance the particle has in moving through the fluid, the slower the particle moves along these streamlines and the more time they spend near the bubble, the more time inertial and gravitational forces have to drive the particle towards the bubble surface. This zone is part of the collision process [14].
In the second zone, a strong electric field is present due to the non-equilibrium distribution of ions around the bubble. This either attracts or repels the particle from the bubble surface, depending on the ion distribution and the charge of the particle. In addition to these electrophoretic forces, diffusional forces are present in the second zone. For sub-micron particles the diffusional and electrophoretic forces are stronger than the gravitational and inertial forces and must not be neglected. This zone is also part of the collision process [22].
The third zone is where surface tension forces become of influence and where particle-bubble attachment takes place. Depending on the sign of the total force, the thin liquid film between the particle and the bubble surface may become thinner more quickly, more slowly or not at all, and therefore, the attachment of particles to the bubble surface may be promoted or prohibited [23].

Now that the different divisions of particle-bubble attachment in equation 2.2 have been explained, an expression for the flotation recovery can be formulated. The flotation recovery R is given by equation 2.2 [20]:

$$R = R * (1 - e^{(-kt_b)}, \tag{2.4}$$

where $R*$ is the maximum particle flotation recovery, t_b is the bubbling time and k is the flotation rate constant given by equation 2.2,

$$k = \frac{3Q_g E_c E_a E_s}{2d_b A_c}, \tag{2.5}$$

where the volumetric gas flow rate Q_g is a predefined value depending on the desired flow, and A_c is the cross-sectional area of the bubble column. The particle diameter d_b is a property that can be determined experimentally.

From equation 2.2, a recovery curve is expected that rises quickly when the bubbeling is commenced, then reaches an asymptote at the value of maximum recovery $R*$.

2.3. Interaction of bubbles with a filter

When using a filter in a fluid reservoir, pressure can build up at one side of the filter. Surface tension forces hold water in the pores of the filter, such that no gas can pass through. The point at which the pressure is high enough to force air through the largest pores in the filter is called the bubble point. At pressures below the bubble point,

gas passes across the filter only by diffusion, but when the pressure is high enough to dislodge liquid from the pores, bulk flow begins and bubbles will be seen [24].

2.4. Behaviour of nanoparticles

It has long been known that particle flotation is effective for particles in the 10-200 μm size range [25][26][27]. However, for finer particles, the collision rate and encounter efficiency is significantly lower, and thus the particle flotation is far less effective. However, for particles in the size range 10-100 nm, Brownian diffusion enhances the collection of these particles by bubbles [28], and the particle collection efficiency by Brownian diffusion increases with decreasing particle size.

As shown by Nguyen, George and Jameson, the collection efficiency has a minimum at the particle size in the order of 100 nm, see figure 2.3 [29]. They concluded that for particles larger than this transition size of 100 nm, the inertial forces dominate in particle collection by bubbles, while below this size limit, the diffusion forces control particle collection.

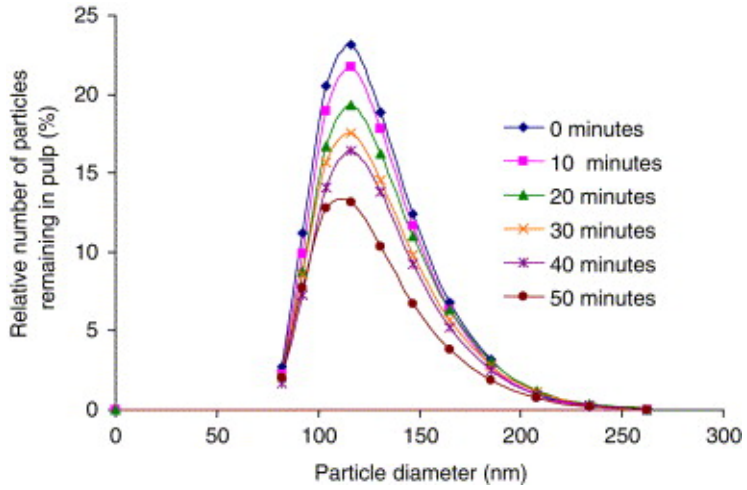

Figure 2.3: Percentage particle number distributions for the Snowtex ZL pulp taken at different flotation time as recorded by Nguyen et al [29]. There is a clear minimum in the particle recovery around 100 nm.

Little information is known about the expected size of fission product particles in the MSFR, but previous experience with MSRs suggests particle diameters approx. between 10^{-9} and 10^{-6}m should be expected [30][31], so expectedly the particles will fall into the size range of particles researched by Nguyen, George and Jameson.

It must be noted that if nanoparticles are smaller than 100 nm, they can become airborne, and possibly be dangerous to human health if they end up in the respiratory system [32].

3

Methodology

3.1. Selection of simulant materials

As the use of actual molten fuel salt (FLiNak) was impossible for this experiment, simulant materials with properties as close to the fuel salt as possible are chosen.
Firstly, the flotation process is only weakly influenced by the used gas due to its low density compared to the density of the fluid [33]. In this setup, air is used because of the conveniency, as pressured air was already available in the laboratory. In a MSFR, an inert gas like helium must be used to avoid processes like oxydation, as the molten salt is very reactive [12].
The most important parameters to take into account for the particle selection are the density, particle size and particle hydrophobicity. As there are a variety of particles in the MSFR and their size (ranging from a few ångströms to a few microns) is still a matter of discussion [34], particles with different size and density have been considered. The choice for the polystyrene particles used in this experiment was made for their hydrophobic behaviour, which is close to the behaviour of the metallic particles in the MSFR, and their fluorescent ability, which makes them ideal to track. The used particles are 250 nm in size and have a density of 1.05 kg/m^3.
Lastly, the simulant fluid must behave similarly to a molten salt when looking at the flotation mechanism and particle collection by bubbles. Important fluid parameters for this are the fluid motion and velocity fields around the bubbles. These parameters are, amongst others, dependent on the dynamic viscosity of the liquid μ_l. Hence, the chosen simulant fluid is 41.6 wt % glycerol, because it closely approximates the dynamic viscosity of the fuel salt (FLiNaK). The bubble formation process can however still be very different because of other properties, namely the liquid density ρ_l and the surface tension σ, play a role due to the temperature differences in the fuel salt [12].

3.2. Experimental setup

In this section, the different parts of the setup used to do the measurements are explained. These three parts are the bubble column, the laser unit and the detection unit. Further, the absorption and emission spectra of the used particles are given.

3.2.1. Bubble column

The cylindrical bubble column gives a way to visually observe the light of the fluorescent particles. The column is made of polymethyl methacrylate (PMMA) or Perspex®. Lakerveld observed that using a cylindrical glass column gave much distortion of the image at the edges of the cylinder [14]. The current column is square on the outside and has a separate cylindrical column on the inside. The square column is filled with demineralised water, and the cylindrical column with the simulant fluid. Lakerveld observed that perspex-water interface between the water and the cylindrical column gives far less distortion because of smaller differences in refractive index. No distortion was present in the measurement area, whereas when using a single cylindrical column distortion was a major issue at the edges of the column.

The gas needed for the experiment is provided by the compressed air system in the laboratory. A mass flow controller (Bronkhorst ELFlow Select) is used to control the gas flow from 10 to 500 sccm or cm^3/min [35] with 0.5% accuracy. The gas is led into a pressure chamber underneath the column, and the bubbles are then formed by a bubble sparger (metal sintered filter, SIKA-R3 with 26 mm diameter, a thickness of 3 mm and a 3 µm average pore size [13]).

At the top of the column, the floated particles have to be collected. The effectivity of three methods has been studied: the evaporation of particles at the fluid-air interface, the use of a Hallimond tube and the use of filter paper. The effectivity of the collection method is measured by the reduction of particle concentration over time.

In figure 3.1, the bubble column is shown with the filter on top. A piece of filter paper is trapped inside the grey connection piece between the column and the glass cylinder. The blue tube is the gas inlet. Figure 3.2 shows the column with the Hallimond tube on top. A simulation of the streamlines in the Hallimond tube is shown in figure 3.3. As can be seen in figure 3.3, in the conical tube reservoir, there is very little fluid motion.

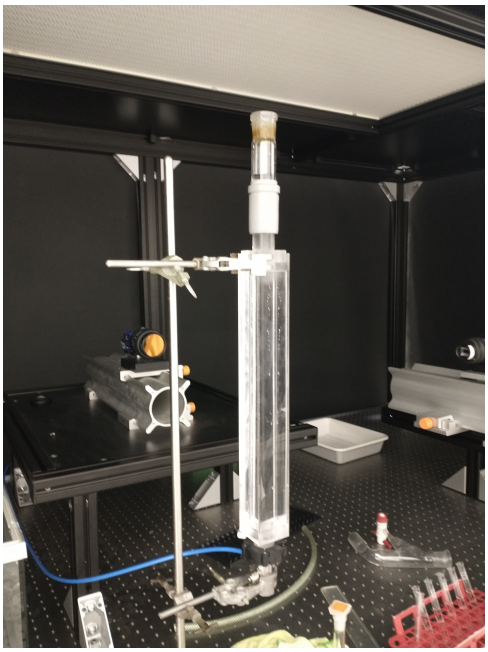

Figure 3.1: The measurement column with filter attached.

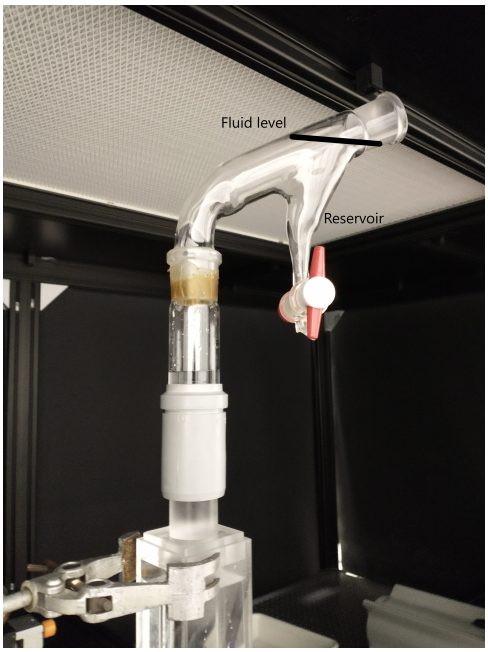

Figure 3.2: The column with hallimond tube attached. Indicated are, in a black line, the fluid level, and the reservoir.

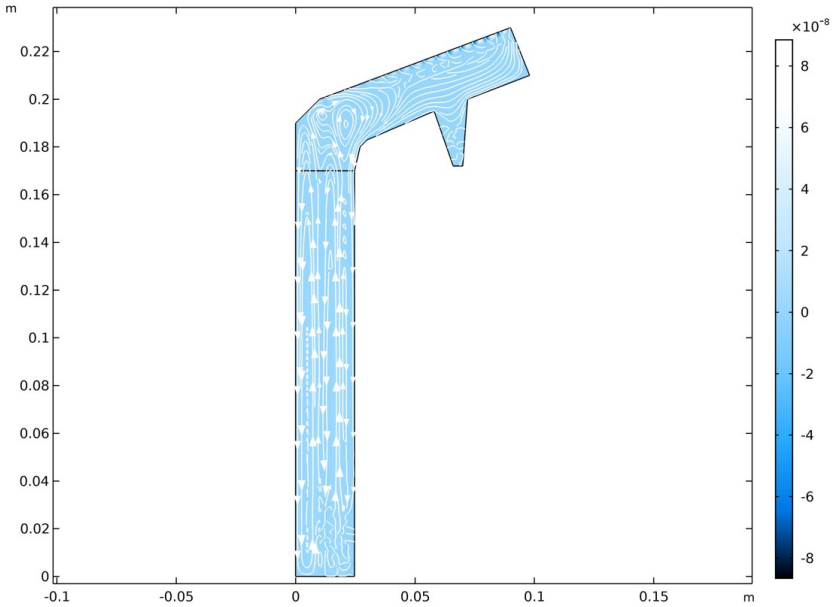

Figure 3.3: Simulation of the streamlines in the Hallimond tube in Comsol Multiphysics, the white arrows indicating the streamlines. In the conical tube reservoir, there is very little fluid motion. Made by Thomas Dumaire, used with permission.

3.2.2. Laser

For imaging of the fluorecscent particles, a technique called Laser Inducent Fluorescence, or LIF, is used. LIF enables concentration, mixture fraction and temperature measurements in fluid mechanical processes. In these experiments, only concentration measurements are used.

LIF imaging consists of two steps: a laser photon is absorbed by a particle, which then emits a fluorescent photon. The emitted photon has a different wavelength than the laser photons, so an optical filter is used to select only the emitted wavelengths. It must be noted that not all absorbed photons result in an emitted photon, some particles relax without emitting a fluorescent photon, and only a fraction of the emitted photons are collected by the detection device. Figure 3.4 shows a schematic of the LIF setup.

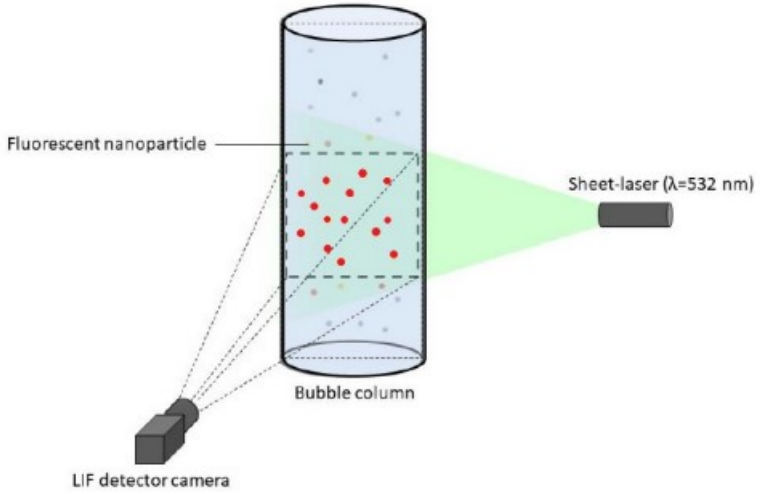

Figure 3.4: A schematic overview of the setup for the LIF measurements. The green area represents green light from the laser sheet incident on the fluorescent particles, that due to this emit red light in all directions so that a LIF detector camera is able to detect the particle concentration [13].

To be able to have a 2D image of the column without layering, a sheet laser is used. In most systems, a light sheet is formed by using a cylindrical lens. When used alone, a cylindrical lens only expands the beam in one direction, with no control over the beam width. A spherical lens is used to focus the light into a thinner sheet in the measurement area [36]. Figure 3.5 shows a schematic of the side and top views of the laser light. Also shown is a light intensity distribution in the sheet. As can be seen, the light is most intense at the midpoint of the sheet.

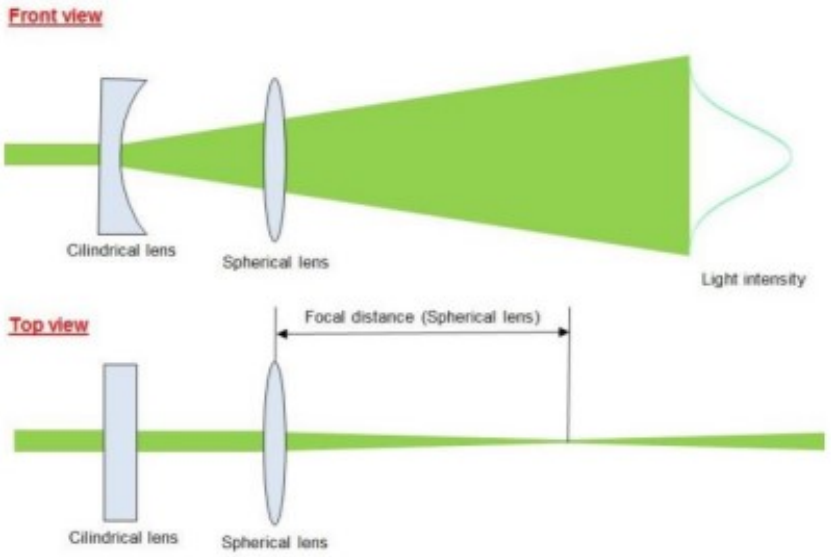

Figure 3.5: Sheet optic schematic using a cylindrical and a spherical lens [36].

The laser model used during the experiments is PSU-H-FDA provided by LaVision (Figure 3.6). This is a Nd:YAG (neodymium-doped yttrium aluminum garnet; Nd:$Y_3Al_5O_{12}$) laser sending out 532 nm green light. For the different measurement tasks output energies up to 400 mJ per pulse are available. Pulse rates of 10 Hz are used for gaseous and liquid fluid applications like this experiment. The laser is a Class 4, the highest and most dangerous class of lasers. Class 4 laser light, whether direct, indirect or diffuse, can burn skin and/or cause permanent eye damage. It is therefore necessary to remove reflective materials such as jewelry or watches and wear protective laser goggles while operating the laser.
It must be noted that the first one to two seconds, the laser is heating up, and the first 10 or so images are increasing in concentration, and are not representative. Therefore, it must be decided per series of 50 images from which image the measured concentration has stabilised and the images before discarded.

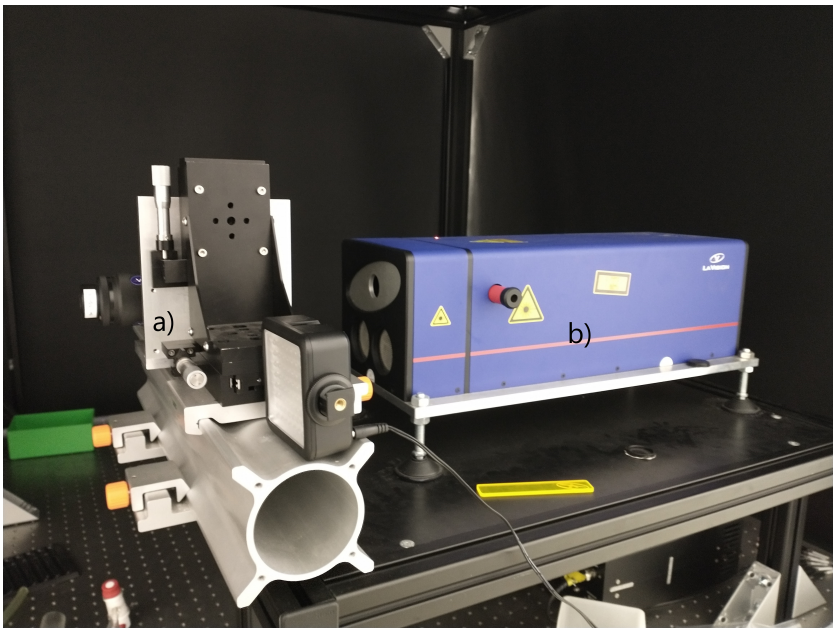

Figure 3.6: The laser system used to excite fluorescent particles, consisting of the sheet lens optic a) and the generation unit b).

3.2.3. Detection

To detect the fluorescent light, a time-gated digital camera with an optic filter is used. The conversion of LIF images into meaningful concentration images is based on calibration measurements, which shall be discussed in the next section. The camera model is an Imager MX 4M (2048 x 2048 pixels) that combines high spatial resolution with a high framerate. When the LIF-filter is on, the ratio of the camera's focal length to the aperture diameter is set such that as much light as possible is detected to make an image.

3.2.4. Exitation and emission spectra

The used fluorescent nanoparticles are Nile Red by Spherotech. Spherotech provides exitation and emission curves, presented in figure 3.7. Based on this, the used optical filter is a 600 nm ± 25 nm filter.

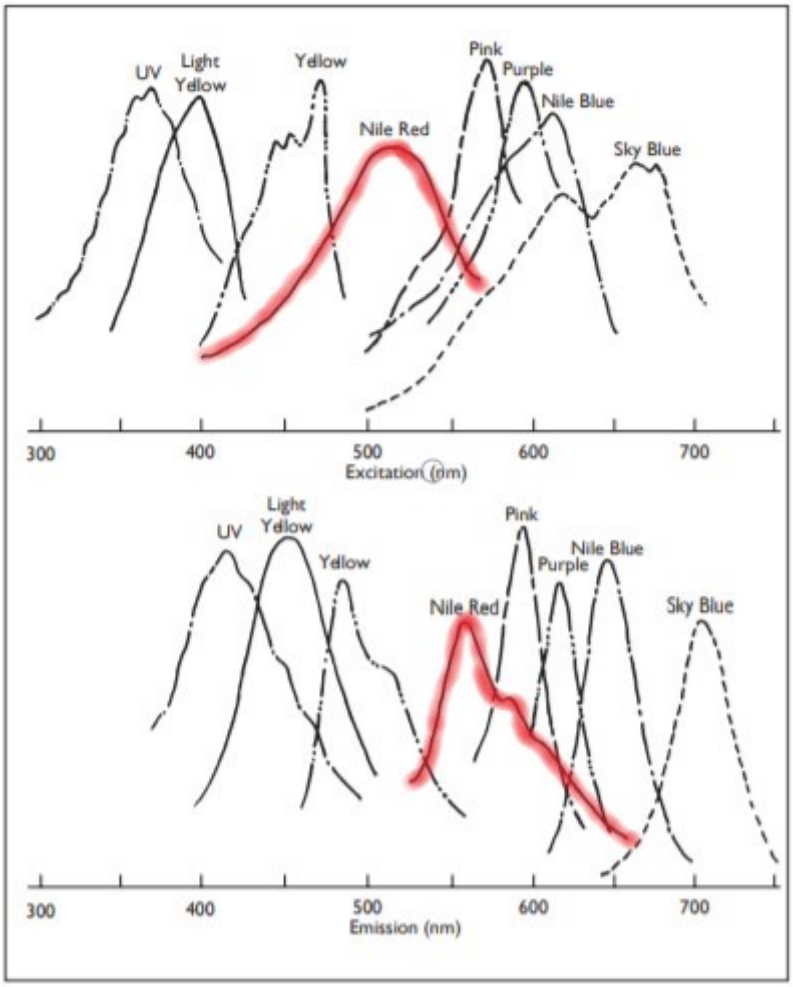

Figure 3.7: Exitation and emission curves for different fluorescent particles, the curves for Nile Red particles are arcaded in red. The excitation peak of Nile Red particles lies around 530 nm, and the emitted light can be detected using a 600 nm ± 25 nm filter [37].

3.3. Image processing

The concentration images compiled by the detection unit have to be processed in order to be able to correct for noise that may be present in the original image. Because the particles are sub-micron scale, a single particle cannot be detected. Rather, what is detected is the fluorescent light of an agglomeration of the particles, the intensity of which is registered in grey scale count. In subsections 3.3.1 the calibration of the relative concentration is explained and in 3.3.2 the several image processing steps are presented.

3.3.1. Concentration calibration

To be able to say something about the extraction rate of the particles from the column in percentages, a calibration curve has to be constructed of the form $C = a * I$, with C the relative concentration, a a constant that determines the slope of the calibration curve, and I the measured intensity. To do this, prior to a measurement, samples with a pre-determined relative concentration, say 20%,40%,60%,80% and 100%, are measured while the fluid is at rest. These relative concentrations correspond with an absolute concentration of particles per unit volume.
The calibration curve is then constructed by fitting a straight line to these measurement points, and the constant a is determined. During bubbling experiments, the curve can then be used to determine relative particle concentration by way of $C = a * I$. An example of such a calibration curve is given in figure 3.8.
With the relative concentration known, the absolute concentration of particles per unit volume can be calculated, and over the course of a measurement, the decrease in the amount of particles while bubbling can be determined. While bubbling, the calibration curve is different because of the reflections of fluorescent light in the bubbles. The construction of the calibration curve while bubbling is discussed in section 3.4.1.

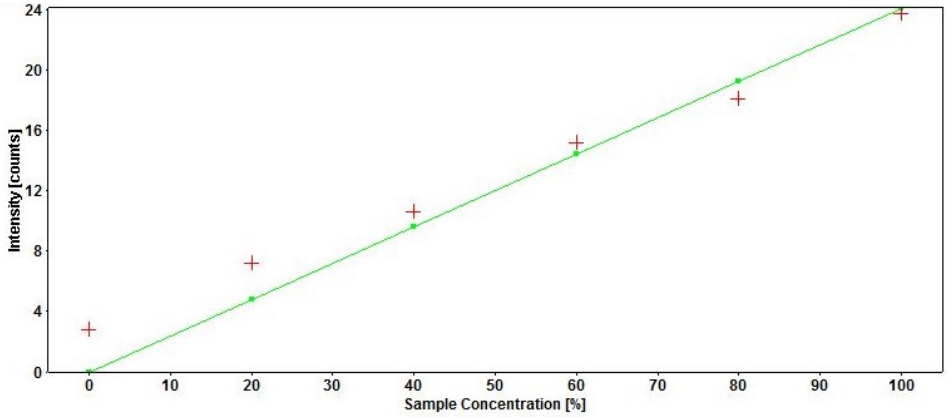

Figure 3.8: Example of a calibration curve obtained prior to an experiment with the measurement points at 0,20,40,60,80 and 100 % and a linear curve of the form C=a*I fitted to the measurement points. During a measurement interpolation is performed to calculate the relative particle (sample) concentration.

3.3.2. Image processing

Before the grabbed images can be interpreted, however, a number of processing steps have to be taken in order to compensate for noise and to calculate the relative concentration . The applied image processing steps are listed below:

- Background subtraction: the camera dark current and the background image from surrounding light add an offset to the grabbed image. To see only the pure LIF image, this background image is removed.
- Sheet correction: as the laser beam is the strongest around the middle line of the image, this causes the intensity to be higher in the middle than at the edges of the image. Also, the optical components of the detection unit will influence the image. These effects are corrected for during this step.
- Image correction: the image distortion, which may have occurred during the previous processing steps, is corrected.
- Concentration calculation: the intensity count of the image is calibrated along the obtained calibration curve, computing a concentration image.
- x-y plot: the average concentration of every image is plotted in a plot of concentration v/s image number. From this, the average concentration for the whole series of images is determined.

The exact procedure to be followed, including screenshots of the processing software DaVis can be found in appendix A1.

3.4. Experimental requirements

Under investigation in this thesis is the behaviour of $250nm$ polystyrene particles under influence of different gas flow rates. The measurement has been constricted to a part of 40 to $50mm$ in the middle of the $605mm$ long bubble column by equipment restraints. It has been verified by Lakerveld that the light intensity profiles in different parts of the column show very similar gradients in their decrease, though the absolute intensity differs. Because only relative decrease is of importance, it is concluded that differences between different parts of the column need not be considered, because their relative decreases are very similar [14]. It is assumed that the measurement location at the middle of the column exhibits the same relative decrease in particle concentration as a location at the top or the bottom of the column would.

From the research of Capelli , it is known that for molybdenum micron-scale particles, the Hallimond tube is effective and that it applies a boundary condition at the top of the column, where particles are removed at a certain rate [12]. The efficiency of the Hallimond tube for the sub-micron polystyrene particles is discussed in Chapter 4.2.2.

Based on equation 2.2, it is expected that maximum particle recovery is achieved at $t = \infty$, and so that a longer bubbling time will result in a higher particle recovery. Due to the exponential behaviour of the recovery curve, however, the recovery is expected to increase the most in the first 20 minutes. Lakerveld recommended a measurement time of 30 minutes, to increase the amount of experiments that can be done in a certain time, as his own experiments had a measurement time of 60 minutes [14].

It must be noted that the first one to two seconds, the laser is heating up, and the measurement results will not yet be stable. It must be determined per set of 50 images from which image the result is stable, which shall generally be from the 10th image.

3.4.1. Optimisation of the measurement method

From the research of Lakerveld, it became apparent that there were several parameters that had not been taken into consideration but nevertheless influenced the measurement result. Before commencing any concentration measurements, the influence of these parameters on the results first had to be established. The first parameter that was of concern is the temperature of the fluid. As viscosity rises with the decrease of temperature, and viscosity is of influence on the gas holdup, and thus, on the flow regime, changes in temperature can result in unwanted changes in the flow regime. If, as expected by Lakerveld, the inlet temperature of the gas is much lower than the initial temperature of the fluid in the column, the viscosity will increase, with an increase in gas holdup as a result. To research the changing temperature of the fluid with time while bubbling, temperature measurements are done while bubbling at different flow rates. These measurements are done by way of a thermocouple attached to a multimeter, which has an uncertainty of 1 decimal. The setup is shown in figures 3.9 and figure 3.10. The purpose of these measurements is to know what temperature the system stabilises at, and the time needed to reach that stable temperature, for different flow rates. Lakerveld expected that this should be achieved within 30 minutes. Over the course of 30 minutes of bubbling, the temperature is measured every 5 minutes, for flow rates of 5 to 50 sccm in increments of 5 sccm.

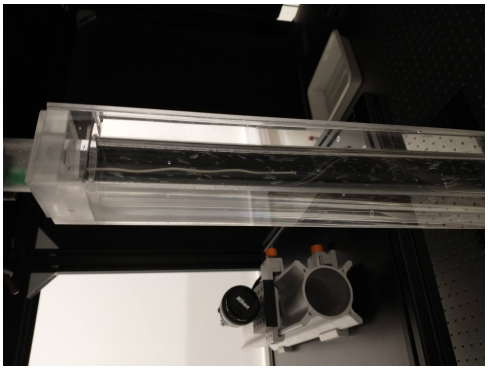

Figure 3.9: The measurement column with the thermocouple at the end of the metal bar.

Figure 3.10: The used multimeter.

Lakerveld also mentioned the effect of bubble reflections on the measured intensity. The fluorescent light reflects in the bubble, augmenting the direct fluorescent light, resulting in a higher measured intensity. To be able to compare between flow rates, this should be corrected for. To establish the relation between flow rate and measured particle concentration, for pre-determined concentrations of 0 to 100% in increments of 20%, the concentration was measured for flow rates of 0 to 35 sccm in increments of 5 sccm. It is expected that with the linear increase of the amount of bubbles, the amount of reflections and thus the measured concentration will also rise linearly. If the curve is indeed linear, as illustrated in figure 3.11, this correction can be done following equation 3.4.1:

$$\text{Corrected concentration} = \frac{(\text{measured concentration}) * \text{pre-determined concentration}}{(\text{flow rate}) * a + b}, \tag{3.1}$$

,where a is the slope of the curve, and b is the offset, which is found by extrapolating the obtained curve and determining the crossing point at the y-axis. The pre-determined concentration is the concentration that is measured in the column at rest. A short derivation for the equation can be found in appendix A.2.1.

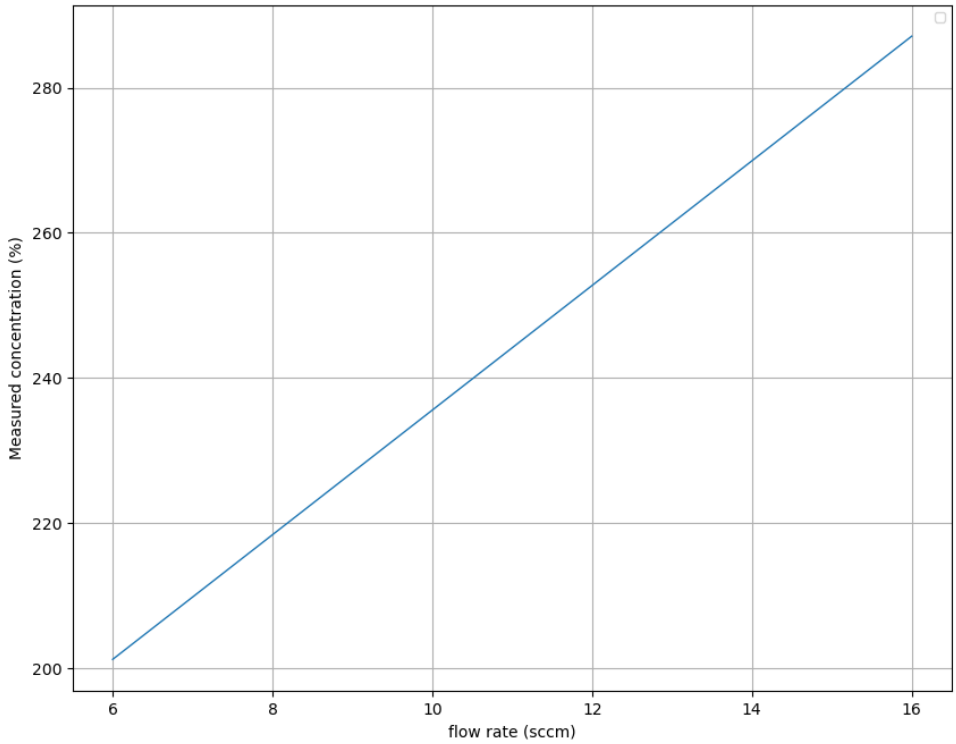

Figure 3.11: Example of a linear bubble correction curve. To determine a, the slope of the curve is found. To determine b, the curve is extrapolated to the y-axis and the crossing point with the y-axis is found.

Lastly, in section 3.2.1, it was noted that the mass flow controller (Bronkhorst EL-Flow Select) could control the flow rate from 10 to 500 sccm with 0.5% accuracy. However, the measurements require flow rates below 10 sccm. To verify whether the mass flow controller works for flow rates lower than 10 sccm, and with what accuracy, the intensity is measured for flow rates 2 to 8 sccm at 100% concentration, and compared with the curve obtained in the bubble reflection measurements discussed above. If the measurements points lie on the extrapolated curve, they are accepted as reliable flow rates. To measure their accuracy, a series of 10 measurements is done to measure the gas holdup at these flow rates. While bubbling, the height of the fluid in the column is measured, then the fluid is left to rest until no bubbles are present anymore. The standarddeviation of the fluid height is a measure for how accurate the mass flow controller is at that flow rate.

3.4.2. Measurement schedule for the particle extraction measurements

After establishing all the parameters that could be of influence on a measurement, the measurement schedule of concentration measurements is made, which can be found in table 3.1. It was decided that to compare the three different extraction methods, measurements would be done in both water and 41.6 wt % glycerol to compare the influence of viscosity. For water, a flow rate of 20 sccm was chosen, while for the glycerol a flow rate of 12 sccm was used because of its higher viscosity and higher gas holdup. As each measurement point consists of 50 images, the average and standard deviation is taken to obtain the measurement value with its error. The measurement points obtained while bubbling are corrected for this, as well as their errors.

The three particle extraction methods are the evaporation of particles at the fluid-air interface, the use of a Hallimond tube and the use of filter paper in the fluid above the measuring point. The evaporation of particles is driven by the mechanism that the concentration difference of particles between the fluid and the air above could cause the particles that have been brought to the fluid-air interface to evaporate and be taken along with air convection. The shape of the Hallimond tube, see figure 3.2 should cause particles that are taken to the fluid-air interface to be captured in the reservoir. The filter paper should either trap the particles in its pores, or the particles pass through and do not return through the filter. The filter must be thoroughly wetted and it must be determined whether the used gas flow rate is above the bubble point. The filter must be replaced between measurements. For all three extraction methods the concentration calibration was done first without the extraction device on top of the column, and additional fluid was added when the extraction device was in place.

Table 3.1: Measurement schedule for determining the particle extraction efficiency of three different methods, in water at 12 sccm, in 41.6 wt % glycerol at 20 sccm, at room temperature. The measurements were done starting from a pre-determined concentration of 100 %

	Water	41.6% wt glycerol
Evaporation of particles at the fluid-air interface	#1	#2
Hallimond tube	#3	#4
Filter paper	#5	#6

4

Results

This chapter presents the results of the experimental work. First, the results of the measurements to determine the influence of certain parameters are presented in section 4.1 and the results of the particle are then discussed in section 4.2.

4.1. Optimisation of the measurement method

In the experiments of Lakerveld, it became apparent that the particle concentration in the column did not show the decrease that was expected by him and the reasons for which could not be found experimentally then. His conclusion was that there were flaws in the method of measuring. Therefore, this section is dedicated to the results of the experiments done to further optimise the measurement method.

4.1.1. Results of the temperature measurements

Temperature measurements are done over a range of flow rates to determine the effect of the temperature of the incoming gas on the temperature of the fluid in the bubble column. The results for water are in figure 4.1.
From figure 4.1, it is apparent that the temperature only varies slightly around room temperature, which was 22°C, and these temperature variations are not dependent on flow rate. If indeed, as expected by Lakerveld, the gas inlet temperature was significantly lower than the fluid (room) temperature, it should be expected that the temperature of the fluid should settle at a lower temperature than room temperature, and that this would be a lower temperature for higher flow rates. From this, it is concluded that in this setup, viscosity changes due to variations in temperature need not be taken into account in further experiments.

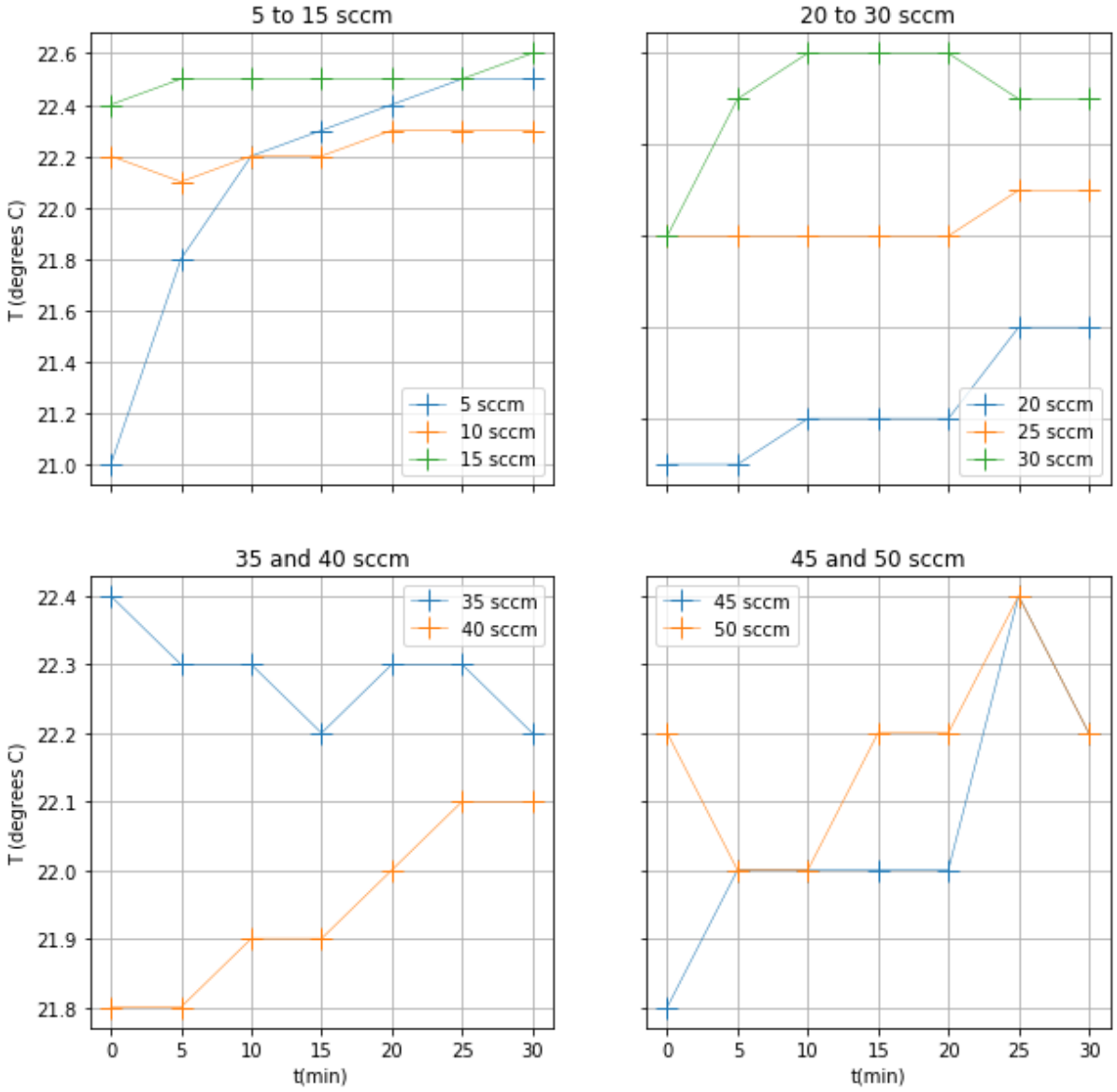

Figure 4.1: Temperature v/s time in water for flow rates 5 to 50 sccm. Uncertainty of the temperature is not shown, but is equal to 0.05 ° C for every measurement point.

4.1.2. Results of the bubble reflection measurements

Concentration measurements are done for a range of flow rates in solutions that range from 0 % to 100 %, measured at 0 sccm. To these measurements, linear bubble correction curves are fitted. Linear curves are used because it is expected that with the linear increase of the amount of bubbles, the intensity of the reflected light should also increase linearly. Figure 4.2 shows the measurement points and fits for water, figure 4.3 those for 41.6 wt % glycerol. The "measured concentration" is the concentration that was measured while bubbling, while the concentrations in the legenda are the pre-determined concentrations that are measured in the solution when the solution is at rest. The pre-determined concentrations are the concentrations that are to be expected when measuring if there was no reflection of fluorescent light by the bubbles.

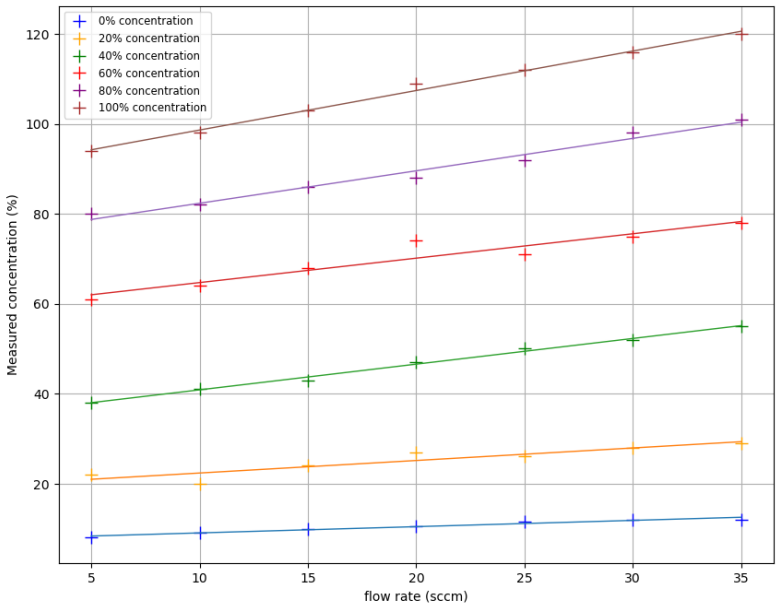

Figure 4.2: Measured concentration versus flow rates 5 to 35 sccm in water with nanoparticles of 250 nm. The bubble concentration curves are fitted to the data points, providing a slope and offset for each pre-determined concentration.

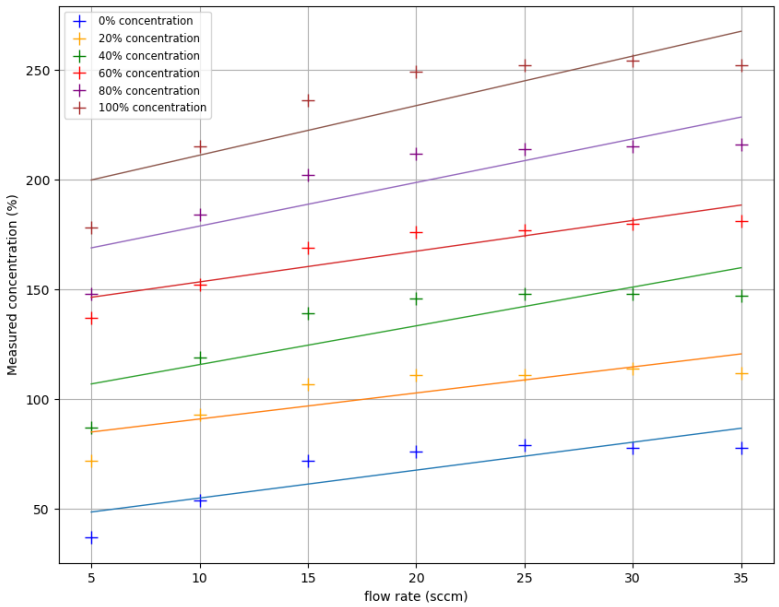

Figure 4.3: Measured concentration versus flow rates 5 to 35 sccm in aqueous 41.6 % glycerol with nanoparticles of 250 nm. The bubble concentration curves are fitted to the data points, providing a slope and offset for each pre-determined concentration.

Figure 4.2 shows that the relation between measured intensity and flow rate is linear in water up to 35 sccm. In figure 4.3, it is also shown that this is not the case for 41.6 wt % glycerol up to 35 sccm. This may be explained by the higher gas holdup in the more viscous 41.6 wt % glycerol. At around 20 sccm, it was not possible anymore to discern any separate bubbles anymore in the bubble column. It was therefore decided that the measurement should be repeated for 41.6 wt % glycerol, but with flow rates from 0 to 16 sccm in increments of 2 sccm. The results of this measurement are in figure 4.4.

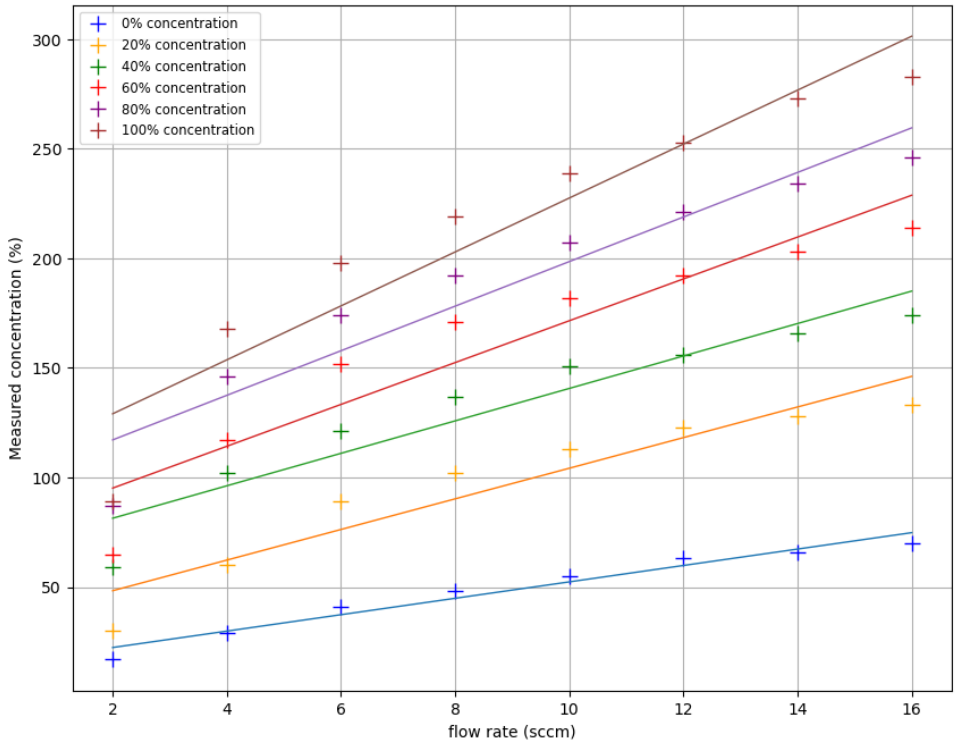

Figure 4.4: Measured concentration versus flow rates 2 to 16 sccm in aqueous 41.6 % glycerol with nanoparticles of 250 nm. The bubble concentration curves are fitted to the data points, providing a slope and offset for each pre-set concentration.

It is apparent in figure 4.4 that from 6 to 16 sccm the measured concentration is linearly dependent on the flow rate, but for 2 and 4 sccm the measurement points do not fit the linear curve. Both from figure 4.4 and from visual observation of the bubble column, it is apparent that the mass flow controller is not reliable for 2 and 4 sccm, as there were only a few visible bubbles in the column and the measured concentrations do not scale linearly with the expected amount of bubbles, which is the case for measurement points from 10 to 16 sccm, for which the mass flow controller is known to be reliable.

4.1.3. Accuracy of the mass flow controller

As relied in chapter 3.4.1, the mass flow controller (Bronkhorst EL-Flow Select) can control the flow rate from 10 to 500 sccm with 0.5% accuracy. For the measurements done here, it is desirable to go below 10 sccm. As was stated in the previous section, for 2 and 4 sccm the mass flow controller is not deemed reliable. Only the accuracy of the mass flow controller at 6 and 8 sccm therefore had to be investigated more carefully. The gas holdup measurements showed an error of 0.40 % and 0.15 % for 6 and 8 sccm, respectively. As these values are both below 0.5 %, it was decided that the accuracy of all used flow rates should be taken 0.5 %. This results in the following plot for 41.6 wt % glycerol:

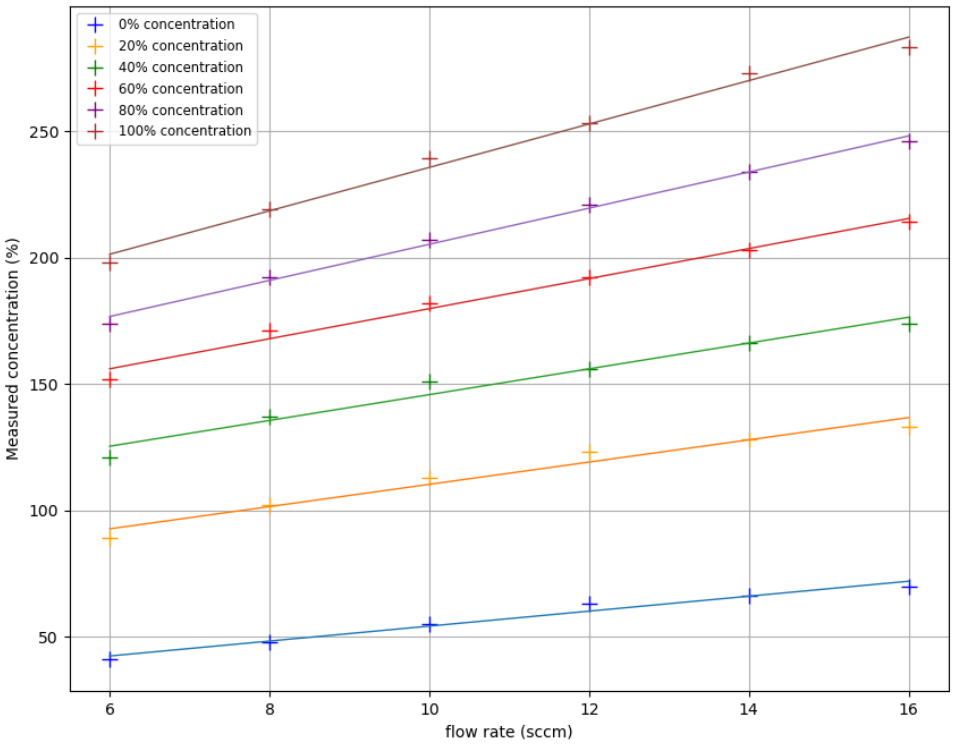

Figure 4.5: Measured concentration versus flow rates 6 to 16 sccm in aqueous 41.6 % glycerol with nanoparticles of 250 nm. The bubble concentration curves are fitted to the data points, providing a slope and offset for each pre-set concentration.

The script for calculating the mass flow controller percentage error from the gas holdup differences and table with all slopes and offsets for both water and 41.6 % glycerol can be found in appendix A.2.

4.2. Results of the particle extraction measurements

To study the process of particle extraction by bubbling, concentration measurements are done in de middle of the bubble column. It is investigated whether there is any decrease in intensity coming from the fluorescent nanoparticles for the three extraction methods. The nanoparticles used have an average diameter of 250 nm. It is expected that the intensity will decrease when bubbling time increases since particles are collected and captured elsewhere. Prior to starting the bubbling, a measurement was taken while the fluid was at rest, this is the measurement at −5 minutes. In a bubbling period of 30 minutes, a concentration measurement was done every five minutes, after which the fluid was left until it was at rest once more, and another measurement was done, this is the measurement point at 35 minutes. When the fluid was once again at rest, another measurement was done. After correction of all measurement images as described in section 3.3.2, bubble reflection corrections were done on the measurements taken while bubbling, as described in chapter 3.4.1, and errors were determined.

4.2.1. Results of the evaporation of particles at the fluid-air interface

The first method that was investigated was the evaporation of particles at the fluid-air interface. According to this method, the nanoparticles should evaporate into the air because of concentration differences and then be taken along the air streams in the lab. It was not expected that this method should work, as the 250 nm particles are too large to evaporate[32]. However, it was neccessary to check as more measures had to be taken to properly calibrate the measurements if evaporation should take place, as well as more protective measures. The results of these measurements are in figure 4.6. Concluded from this is that this method is not efficient, as there is no monotonous decline in concentration.

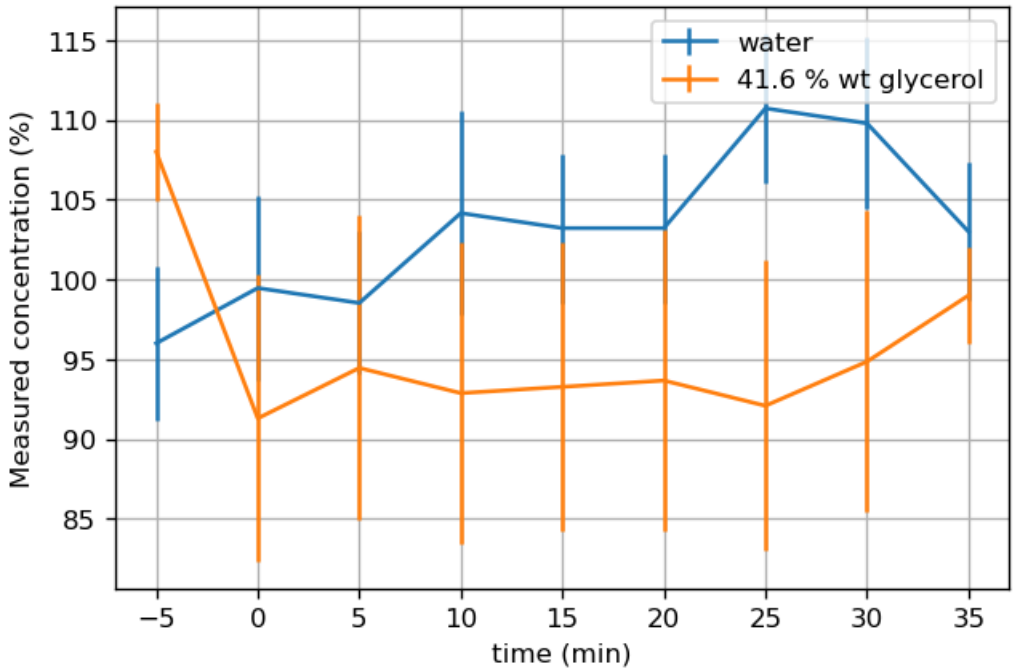

Figure 4.6: Plot of concentration before the bubbling is started (the measurement point at -5 minutes), during bubbling (the measurement points at 0 to 30 minutes) and after the bubbling is stopped and the fluid is at rest once more (the measurement point at 35 minutes). The measurements were done in 41.6 wt % glycerol at 12 sccm and water at 20 sccm with the evaporation of particles at the fluid-air interface as the extraction method.

4.2.2. Results of the Hallimond tube

Secondly, the efficiency of the Hallimond tube is investigated. The shape of the tube should cause the particles to settle in the reservoir when the bubble that carries them reaches the water-air interface. The measurement results are in figure 4.7. It was found strange that when the bubbeling is stopped, the concentration should drop so abruptly, as it was either expected that the concentration should decrease monotonously over the course of the experiment, or that there should be no decrease at all. It was therefore decided that the fluid that is added after the Hallimond tube is put into place should have the same particle concentration as the fluid already in the column. This is done to avoid the sharp drop if it is caused by mixing of the concentrated fluid in the column and the less

concentrated fluid in the Hallimond tube. The results are in figure 4.8. The comparison of figures 4.7 and 4.8 clearly shows that that, indeed, the sharp drop was caused by the mixing of the concentrated fluid in the column and the less concentrated fluid in the Hallimond tube. This method is shown to be inefficient in extracting the polystyrene nanoparticles, as there is no monotonous decline in particle concentration.

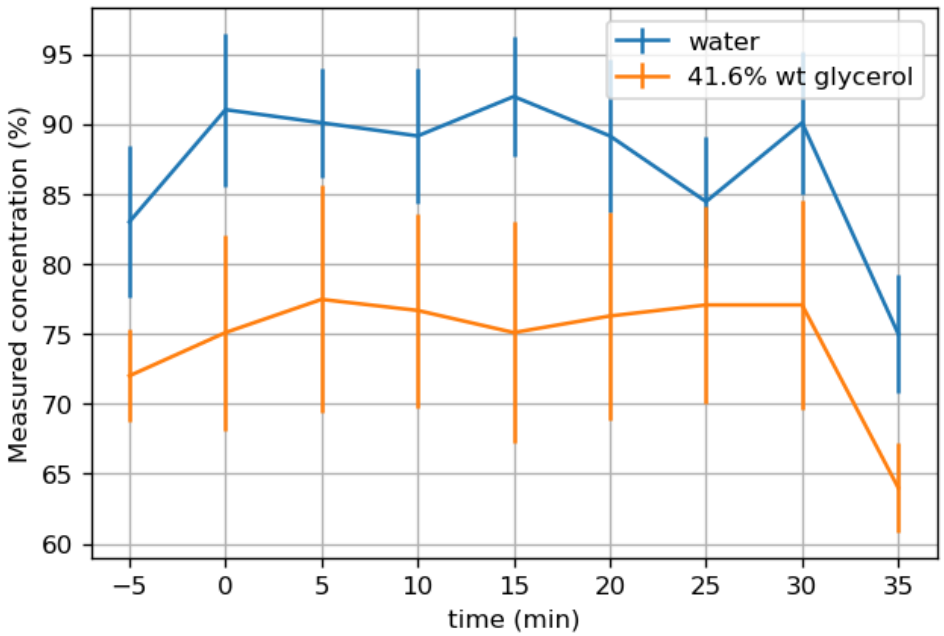

Figure 4.7: Plot of concentration before the bubbling is started (the measurement point at -5 minutes), during bubbling (the measurement points at 0 to 30 minutes) and after the bubbling is stopped and the fluid is at rest once more (the measurement point at 35 minutes). The measurements were done in 41.6 wt % glycerol at 12 sccm and water at 20 sccm with the Hallimond tube on top of the column

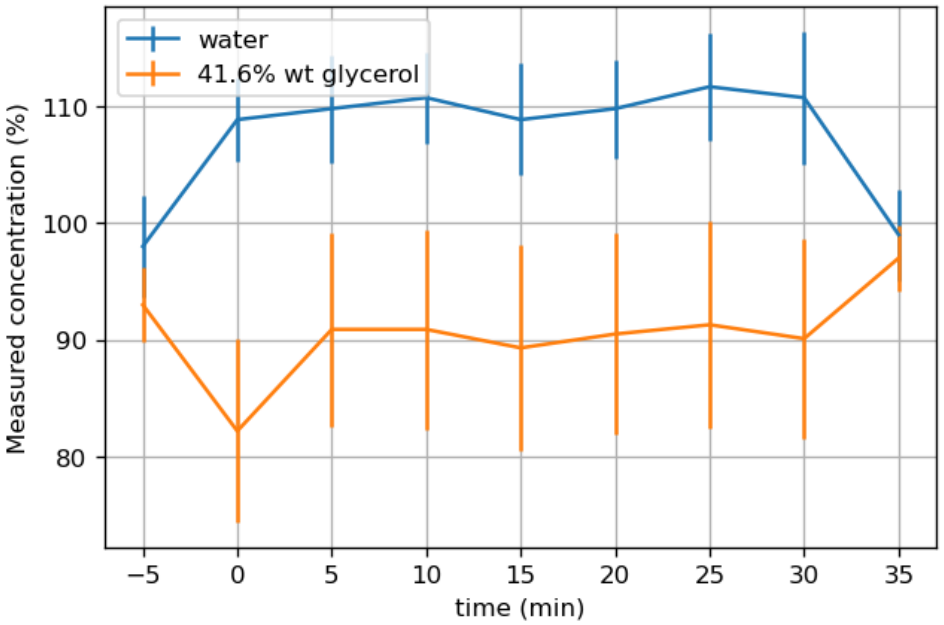

Figure 4.8: Plot of concentration before the bubbling is started (the measurement point at -5 minutes), during bubbling (the measurement points at 0 to 30 minutes) and after the bubbling is stopped and the fluid is at rest once more (the measurement point at 35 minutes). The measurements were done in 41.6 wt % glycerol at 12 sccm and water at 20 sccm with the Hallimond tube on top of the column. The fluid added when the Hallimond tube is installed has the same concentration as the fluid already in the column.

4.2.3. Results of the filter paper

The last investigated method was the use of filter paper in the bubble column. The particles should be either trapped in its pores, or the particles pass through and do not return through the filter. If also the gas would be trapped underneath the filter that could significantly disturb the flow. To determine how the filter influenced the gas and pressure buildup under the filter, it was checked whether there was bubbling above the filter at the used gas flow rates. It was verified that there was bubbling both below and above the filter at the used gas flow rates, so the used gas flow rates cause pressures above the bubbling point. This means that there is pressure buildup below the filter, but the pores of the filter are large enough to let air through at the used flow rate. Then, concentration measurements were conducted, of which the results are in figure 4.9. Again, the fluid that is added after the filter is in place has the same concentration as the fluid already in the column. In 41.6 wt % glycerol, this method is clearly not effective, but in water, it showed a continously declining trend, though within the uncertainties of the measurement points. Another measurement was conducted in water to confirm this trend. To ensure that the measurements were independent, the column was cleaned and filled again with clean water, after which a new concentration calibration, as described in chapter 3.3.1. Also, the filter paper was replaced. The comparison between the two measurements is in figure 4.10. Unlike measurement 1, measurement 2 does not show a continously declining trend, and also the second measurement has a far higher relative concentration. As the first measurement could not be reproduced, it must be concluded that this method with this type of filter is also not effectively removing particles.

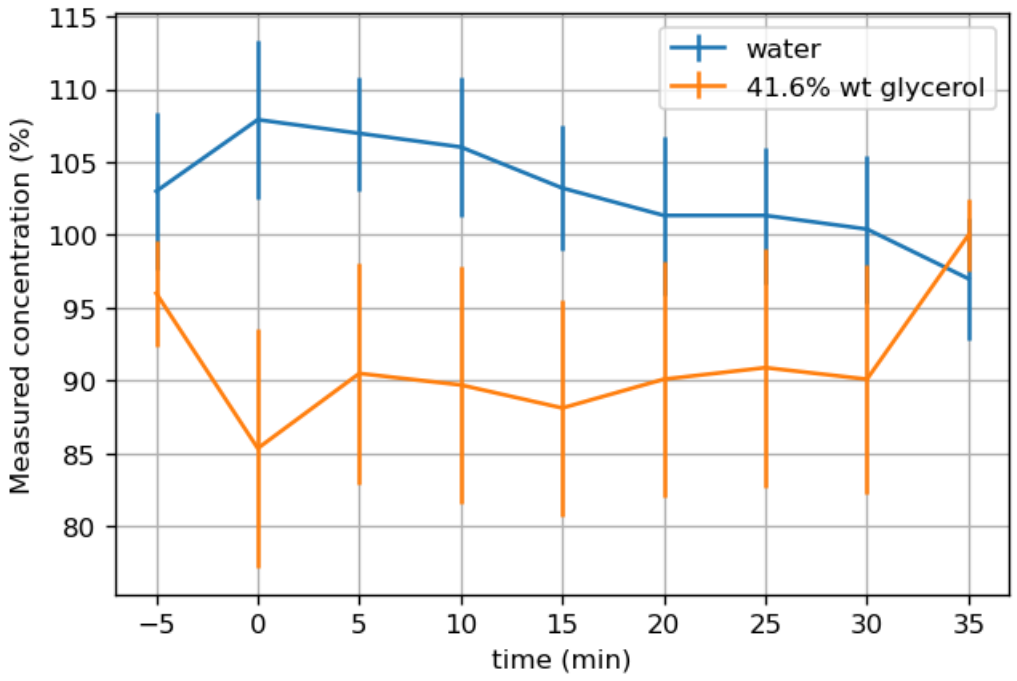

Figure 4.9: Plot of concentration before, during and after bubbling in 41.6 wt % glycerol at 12 sccm and water at 20 sccm with filter paper in the bubble column.

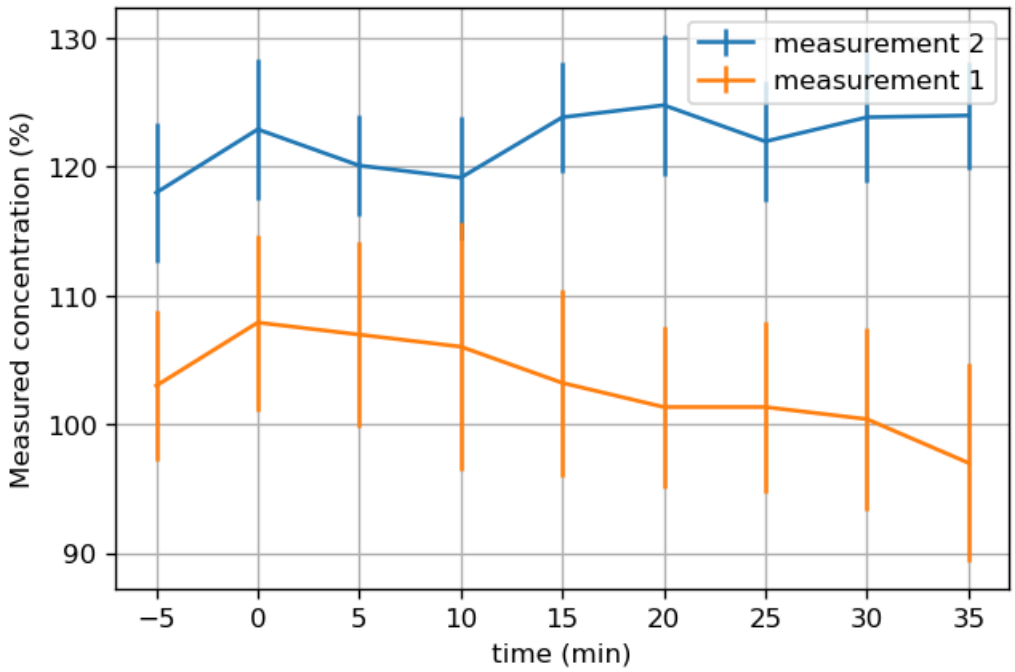

Figure 4.10: Plot of concentration before, during and after bubbling water at 20 sccm with filter paper in the bubble column. Comparison of two independent measurements.

5

Discussion

In this chapter an attempt at interpreting the results presented in chapter 4 is made. The chapter is divided in five sections: the results of the measurements done to optimise the measurement method in chapter 4.1 are discussed in section 5.1. Sections 5.2 to 5.4 are dedicated to the different extraction methods, and section 5.5 will give some suggestions on how to improve further research.

5.1. Optimisation of the measurement method

5.1.1. Temperature measurements

First, the results of the temperature measurements are discussed. It is concluded form figure 4.1 that hat the temperature only varies with 1 °C around room temperature, which was 22°C, and these temperature variations are not dependent on flow rate. From figure 4.1, it can also be seen that the temperature varies slightly nevertheless, and that it rises, rather then falls. This can be explained by either that the air that is supplied by the building is warmer than room temperature, or that the room and thereby fluid temperature is heightened by the body heat of the person doing the experiments, as the laboratory is a well-isolated and not too large room. However, as concluded before, in this setup, viscosity changes due to variations in temperature therefore do not need to be taken into account in further experiments, and this was therefore not further investigated.

5.1.2. Flow rates

In sections 4.1.2 and 4.1.3, it was stated that the decision to limit the flow rates from 6 to 16 sccm for 41.6 wt % glycerol was for lower flow rates due to an unreliable amount of bubbles when the mass flow controller was set lower than 5 sccm. For higher flow rates, the amount of bubbles became so high that the increase in measured concentration due to reflected light was not linear anymore with the flow rate.

5.1.3. Mass flow controller

As discussed in section 4.1.3, the mass flow controller can be properly used from 6 sccm upward, as for lower set flow rates the gas holdup does not correspond with the expected gas holdup. The specifications of this particular mass flow controller, the Bronkhorst ELFlow Select, state that the mass flow controller is reliable from 10 sccm to 500 sccm with an accuracy of 0.5 %. As the accuracies for 6 and 8 sccm fall within this 0.5 %, those flow rates can be used reliably as well.

5.2. the evaporation of particles at the fluid-air interface

As expected beforehand, the evaporation of particles at the fluid-air interface method was not effective to extract particles. For the nanoparticles to become airborne, they need to be smaller then 100 nm, as discussed in chapter 2.4. It is therefore logical that the used particles of 250 nm should not become airborne (evaporate). It is nevertheless good to know that the used particles are not evaporating, as this would disturb the concentration calibration, and as no protective measures were taken to prevent inhaling of nanoparticles.

5.3. Hallimond tube

As the research of Capelli stated that the Hallimond tube worked for micron-scale molybdenum particles[12], and Lakerveld stated that the Hallimond tube worked for the used nanoparticles as well [14], it was unexpected, at first, that the Hallimond tube was not efficient in extracting particles. However, the used polystyrene particles have approximately the same density as the used simulant fluid, so gravity does not play a role in the sedimentation of the particles in the reservoir of the Hallimond tube, as it did for Capelli's metallic particles. Because of the density similarities, the particles follow the fluid stream, and as can be seen in figure 3.3, the fluid streams do not trap the particles in the reservoir, as the fluid in the reservoir is still. Instead, the particles are taken back to the column.

5.4. Filter paper

In section 4.2.3, it was found that there was no buildup of gas or pressure under the filter paper**!!**. As the continously declining trend of the first water measurement could not be reproduced, it was concluded that in glycerol as well as in water, this extraction method with the current technique and filter type is inefficient. Possible explanations may be: the filter paper, which is cellulose and lignin, may react with the glycerol, and the glycerol may take up the site of chemical bonding which would be expected to adsorb the particle. Alternatively, the paper may become saturated with water, and the repellent surface tension forces between the now hydrophilic paper and the hydrophobic polystyrene particles may inhibit the particles to stick to the paper. If considering the theory that the particles pass through the filter and do not return, the fluid may also have occupied the voids in the filter, which would trap the particles below the filter.

5.5. Recommendations

Based on the results from the experiments done in this research, some recommendations are made for further research.
First, the density of the polystyrene particles was too close to the simulant fluid density for the Hallimond tube to be able to work. The particles that are fission products in the MSFR are metallic, and will therefore have a greater density than the polystyrene particles. To be able to conclude about the efficiency of an extraction method in the MSFR, it is therefore advised to repeat the measurements using, if possible, metallic particles, and otherwise particles with a similar density to the fission products. It would be interesting to see whether the efficiency of the Hallimond tube depends on the particle size or rather on the particle density.

Second, from the temperature measurements it became clear that the room and fluid temperature and the gas temperature were close together, and that in these experiments the changing viscosity due to temperature variations did not need to be taken into account. However, it should not be forgotten that the gas and the fluid still must be of the same temperature if working in other conditions, for example in the reactor itself, where the helium should be pre-heated to the temperature of the fuel salt.

Lastly, it would be interesting to investigate the use of different hydrophobic materials as a particle extractor, as the particles themselves are hydrophobic. The filter paper was a first try in this spectrum, but seemingly not sufficiently hydrophobic and/or unreactive. Also, different filter pore sizes may be investigated to see whether the particles pass through the filter or whether they actually adhere to the filter itself. For use in the MSFR itself, more sophisticated extraction methods may also be researched to extract sub-micron scale particles.

6

Conclusion

Nanoparticles created during the fission process in the MSFR could poison the reaction, agglomerate on the cold parts of the reactor core and cause corrosion. This can, to some extent, be prevented by the removal of these nanoparticles by helium bubbling Therefore, for this thesis, experimental research has been conducted to investigate the efficiency of three different particle extraction methods.

The used method for observing the particles is through fluorescent light, which presents a problem when trying to compare the fluid at rest and the fluid while bubbling. The fluorescent light will reflect in the bubbles, amplifying the light coming from the particles themselves. In order to compare the two states of the fluid, corrections were developed in this work, using flow rate-light intensity calibration curves.

Furthermore, it has been verified that the size of nanoparticles used in this research, 250 nm, cannot become airborne and therefore cannot be extracted by the evaporation of particles at the fluid-air interface. It is also probable that, due to the closeness of the densities of the used polystyrene particles and the simulant fluid aqueous glycerol, the Hallimond tube is not efficient in extracting particles from the bubble column. The used method of using filter paper is also not efficient enough in extracting particles to see any significant decrease in particle concentration. This may be because it is reactive with the simulant fluid, or the particles do not adhere to the paper well because of differences in hydrophobicity.

This work covers the complexity of multiphase flows, from flow regime to bubble-particle attachment, and the LIF technique with which the measurements were carried out. And yet, no efficient particle extraction method has been found. Hopefully, an efficient extraction method can be found, and helium bubbling applied to remove unwanted solid reaction products of sub-micron scale from the MSFR.

Bibliography

[1] U.S. Atomic Energy Commission. *The first reactor*. U.S. Atomic Energy Commission, Division of Technical Information, 1967.

[2] Murray. R.L and K.E. Holbert. *Nuclear Energy*. Butterworth-Heinemann, 2015. ISBN: 978-0-12-416654-7.

[3] *Uranium Enrichment*. https://www.nrc.gov/materials/fuel-cycle-fac/ur-enrichment.html. Accessed: 5-11-2021.

[4] World Nuclear. *Physics of Uranium and Nuclear Energy*. https://world-nuclear.org/information-library/nuclear-fuel-cycle/introduction/physics-of-nuclear-energy.aspx. Accessed: 5-11-2021.

[5] Ch Poinssot et al. "Assessment of the environmental footprint of nuclear energy systems. Comparison between closed and open fuel cycles". In: *Energy* 69 (2014), pp. 199–211.

[6] G. H. Fettus and M.G. McKinzie. *Nuclear Fuel's Dirty Beginnings*. 2012.

[7] R. Dones et al. "Life cycle inventories of energy systems: results for current systems in Switzerland and other UCTE countries". In: *Final report ecoinvent data v2. 0* 5 (2007).

[8] Coaltrans. *Carbon intensity of coal per KWh*. https://www.coaltrans.com/insights/article/ecocarbon-august-2021. Accessed: 5-11-2021.

[9] Nuclear Institute. *Nuclear Energy*. https://www.nei.org/news/2015/land-needs-for-wind-solar-dwarf-nuclear-plants. Accessed: 5-11-2021.

[10] International Atomic Energy Agency. *World's uranium resources enough for the foreseeable future, say nea and iaea in new report*. https://www.iaea.org/newscenter/pressreleases/worlds-uranium-resources-enough-for-the-foreseeable-future-say-nea-and-\iaea-in-new-report. Accessed 5-11-2021.

[11] SAMOSAFER. *Project*. https://samosafer.eu/. Accessed 5-11-2021.

[12] E. Capelli. *Notes on Flotation*. Tech. rep. Delft University of Technology, Dec. 2016.

[13] L. Rozing. *Out-of-core Helium Bubbling in the Molten Salt Fast Reactor*. Master's thesis, Delft University of Technology, August 2020.

[14] I. Lakerveld. *Helium bubbling in the Molten Salt Fast Reactor*. Master's thesis, Delft University of Technology, July 2021.

[15] L.C. Goldenberg, I. Hutcheon, and N. Wardlaw. "Experiments on transport of hydrophobic particles and gas bubbles in porous media". In: *Transp Porous Med* 4 (1989), pp. 129–145. DOI: https://doi-org.tudelft.idm.oclc.org/10.1007/BF00134994.

[16] R. H. Yoon and G. H. Luttrell. "The Effect of Bubble Size on Fine Particle Flotation". In: *Mineral Processing and Extractive Metallurgy Review* 5.1-4 (1989), pp. 101–122. DOI: 10.1080/08827508908952646.

[17] C Kleinstreuer. *Two-Phase Flow: Theory and Applications: Theory and Applications (1st ed.)* Routledge, 2003.

[18] M. Collignon et al. "Modelling fluid flow in active clastic piercements: Challenges and approaches". In: *Marine and Petroleum Geology* 90 (Oct. 2017). DOI: 10.1016/j.marpetgeo.2017.09.033.

[19] L. A. Utracki†. "Temperature dependence of liquid viscosity". In: *Journal of Macromolecular Science, Part B* 10.3 (1974), pp. 477–505. DOI: 10.1080/00222347408215165.

[20] J Ralston and S.S. Dukhin. "The interaction between particles and bubbles". In: *Colloids and Surfaces A: Physicochemical and Engineering Aspects* 151 (1–2 1999), pp. 3–14. DOI: https://doi.org/10.1016/S0927-7757(98)00642-6.

[21] B. V. Derjaguin, S. S. Dukhin, and N. N. Rulyov. "Kinetic Theory of Flotation of Small Particles". In: *Surface and Colloid Science: Volume 13*. Boston, MA: Springer US, 1984, pp. 71–113. DOI: 10.1007/978-1-4615-7972-4_2.

[22] J. Ralston, D. Fornasiero, and R. Hayes. “Bubble–particle attachment and detachment in flotation”. In: *International Journal of Mineral Processing* 56 (1-4 1999), pp. 133–164.

[23] Z. Dai, D. Fornasiero, and D. Ralston. “Particle–bubble collision models — a review”. In: *Advances in Colloid and Interface Science* 85 (2-3 2000), pp. 231–256. DOI: https://doi.org/10.1016/S0001-8686(99)00030-5.

[24] Tadeusz Kudra. “FILTERS AND FILTRATION HANDBOOK 4th Edition (1997) By T. Christopher Dickenson Publisher: Elsevier Advanced Technology The Boulevard, Langford Lane, Kidlington, Oxford OX5 1GB, U.K.” In: *Drying Technology* 17 (1999), pp. 363–364.

[25] A. V. Nguyen and H. J. Schulze. *Colloidal science of flotation*. New York: Marcel Dekker, 2004.

[26] N. Ahmed and G.J. Jameson. “The effect of bubble size on the rate of flotation of fine particles”. In: *International Journal of Mineral Processing* 14 (3 1985), pp. 195–215. DOI: https://doi.org/10.1016/0301-7516(85)90003-1.

[27] W.J. Trahar and L.J. Warren. “The flotability of very fine particles—A review”. In: *International Journal of Mineral Processing* 3 (2 1976), pp. 103–131.

[28] D. Reay and G.A. Ratcliff. “Removal of fine particles from water by dispersed air flotation Effects of bubble size and particle size on collection efficiency”. In: *Canadian Journal of Chemical Engineering* 51 (2 1973), pp. 178–185.

[29] A.V. Nguyen, P. George, and G.J. Jameson. “Demonstration of a minimum in the recovery of nanoparticles by flotation: Theory and experiment”. In: *Chemical Engineering Science* 61 (8 2006), pp. 2494–2509. DOI: https://doi.org/10.1016/j.ces.2005.11.025..

[30] E. Compere et al. *Fission Product Behavior in the Molten Salt Reactor experiment*. Tech. rep. Oak Ridge National Laboratory, 1975. DOI: doi:10.2172/4077644.

[31] A. Di Ronco et al. “An Eulerian Single-Phase Transport Model for Solid Fission Products in the Molten Salt Fast Reactor: Development of an Analytical Solution for Verification Purposes”. In: *Frontiers in Energy Research* 9 (June 2021), p. 311. DOI: 10.3389/fenrg.2021.692627. URL: https://doi.org/10.3389/fenrg.2021.692627.

[32] G. Biskos and A. Schmidt-Ott. “Airborne Engineered Nanoparticles: Potential Risks and Monitoring Challenges for Assessing their Impacts on Children”. In: *Paediatric Respiratory Reviews* 13 (12), pp. 79–83.

[33] E. Delnoij. “Fluid dynamics of gas-liquid bubble columns – A theoretical and experimental study”. PhD thesis. Twente University, 1999.

[34] R.J. Kedl. *The migration of a class of fission products (noble metals) in the molten-salt reactor experiment*. Tech. rep. Oak Ridge National Laboratory, Dec. 1972.

[35] Bronkhorst. *Thermal Mass Flow Meters and Controllers: Instruction manual. EL−FLOW® Select series*. https://www.bronkhorst.com/getmedia/257147fc-7f5d-4628-9a47-0533cf68ac08/917099-Manual-EL-FLOW-Select. November 2020.

[36] R.J. Adrian and J. Westerweel. *Particle Image Velocimetry*. Cambridge, 2011.

[37] Spherotech. *SPHERO^{TM} Fluorescent Particles*. https://www.spherotech.com/2020%20Product%20Detail%20Pages/Spherotech%20Fluorescent%20Particles.pdf. December 2019.

A

Appendices

A.1. Image processing

This section of the appendix goes through the different steps that are necessary to perform image processing on data gathered from concentration measurements in fluids, also denoted as LIF-C. It includes 16 screenshots of the DaVis 8.4 software operation list, where all actions are carefully explained in order. There are five subsections: scaling, background subtraction, sheet processing, concentration calibration and experiment.

We start in the begin menu. Click "New Project", and name it. Click "Ok". It will take you to the new project's main page, which looks like figure A.1 (note that figure A.1 is not a new project, a new project would have a blank left column):

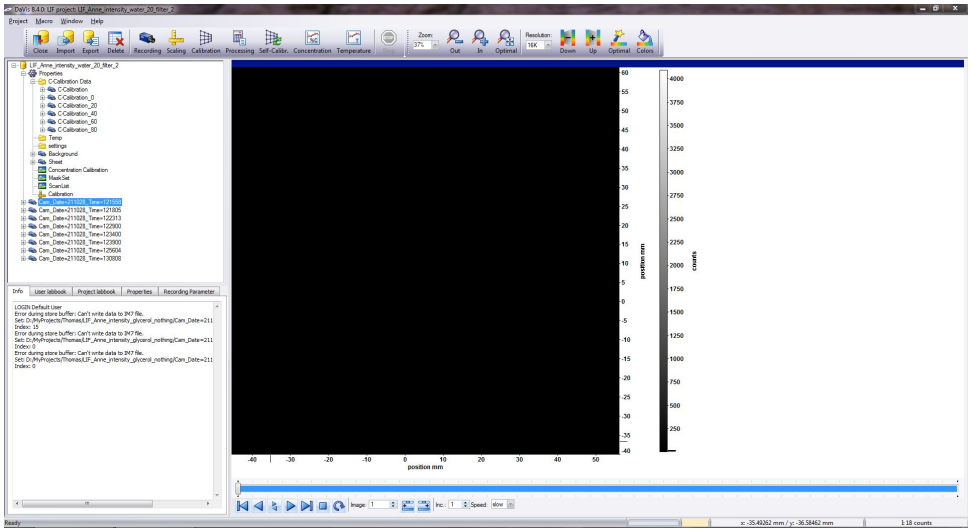

Figure A.1

A.1.1. Focussing

First, the column must be put in front of the laser sheet such that the sheet intersects the column at its widest part. To be able to adjust, click "Recording", see figure. Set illumination to 1000, see figure A.2 and click "Adjust". The laser will now be on constantly. If the column is in the right place, click "Off", so the laser is of. To be able to focus the camera, remove the cap from the camera and put on the LIF-filter. Click "Live mode" and then the right camera icon. This will trigger the camera to continually take pictures. Make sure the laser is off! To focus, turn the ring on the camera closest to the filter. Make sure that the walls of the cylindrical column are sharp in focus.

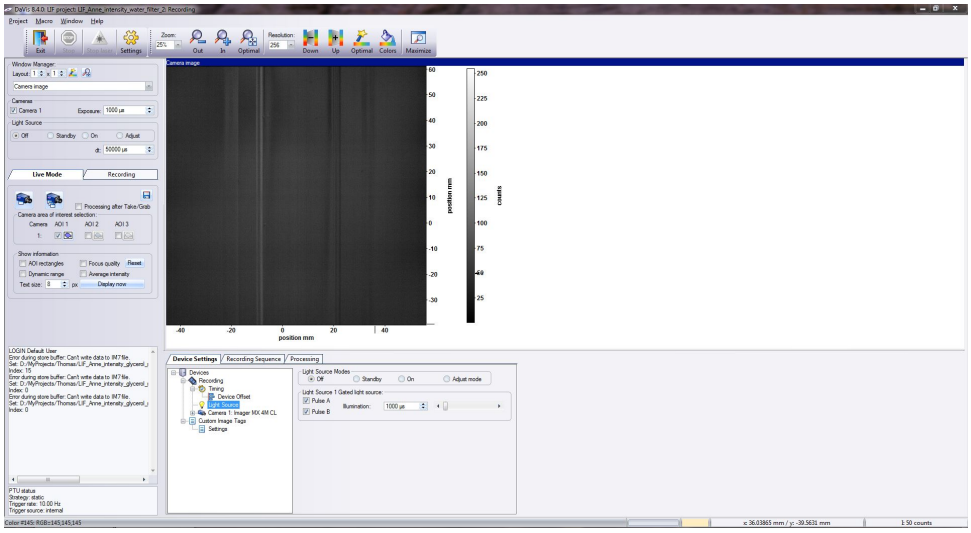

Figure A.2

A.1.2. Background subtraction

The next step is to deal with background noise. The camera's dark current and surrounding light add an offset to the signal from the actual experiment. In order to extract the pure LIF signal these offsets are subtracted by taking 10 images with the lens cap on. In order to do so, click "Recording", see figure A.3 and select "Background images" in the "Recording Mode" dropdown menu. Set "Number of images" to 10. Making sure the laser is "on", click the record button.

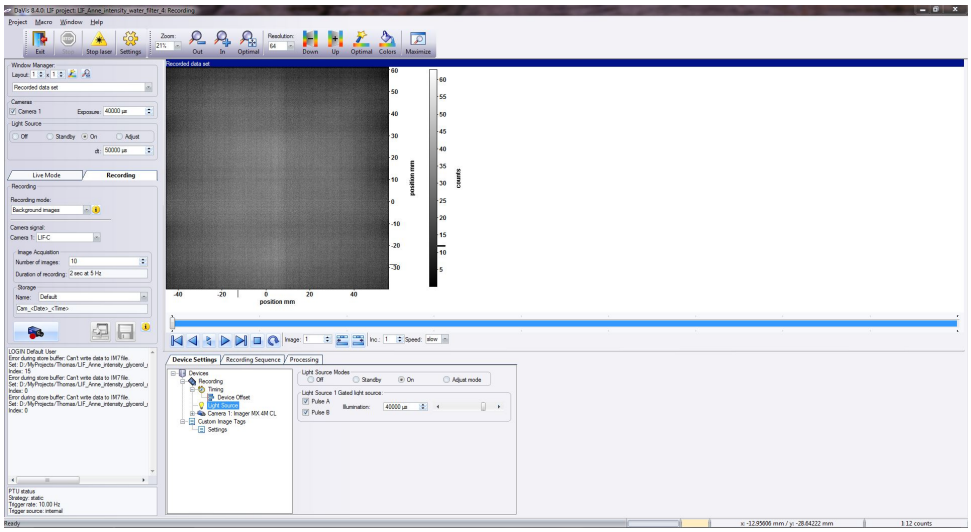

Figure A.3

After the background images are taken, click "Exit" in the top left, taking you back to the project main menu. Select your background image in the left column, see figure A.1 and click "Processing" in the top bar. In the processing menu, see figure A.4, right-click 1. , click "Set operation" and select from "Statistics" "Sum, average, standarddeviation, min, max". Click "Start processing". The image will now be processed and will be visible in the lower right.

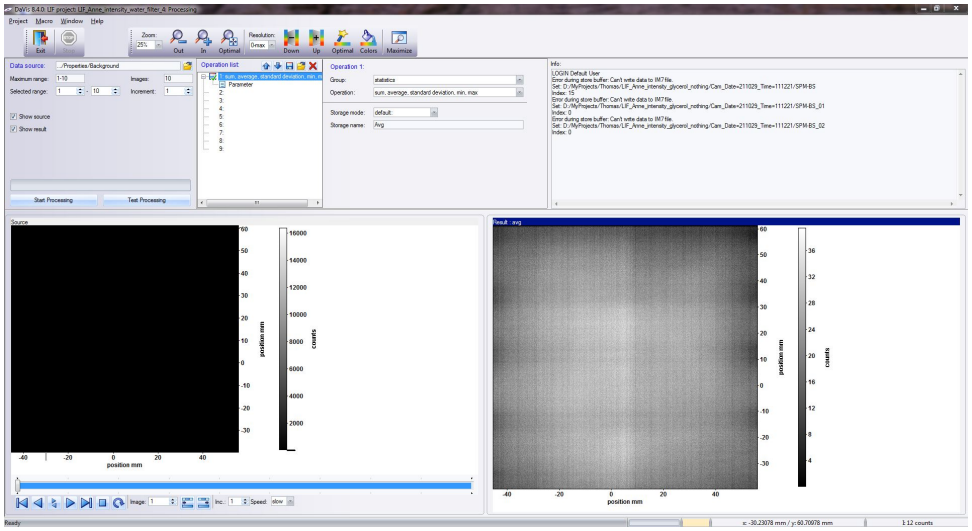

Figure A.4

A.1.3. Sheet processing

The third step takes into account the non-uniformity of the laser illumination. In Figure 3.5 the light intensity distribution is shown to have a Gaussian profile, where in the centre of the light sheet the illumination is maximal. To take care of this non-uniformity, the following steps are carried out. Make sure the laser is turned on at intensity 40000 and the lens cap is removed and put the LIF filter on before starting the recording. Select "Sheet images" in the dropdown menu and set the number of images to 50, see figure A.5. Press record.

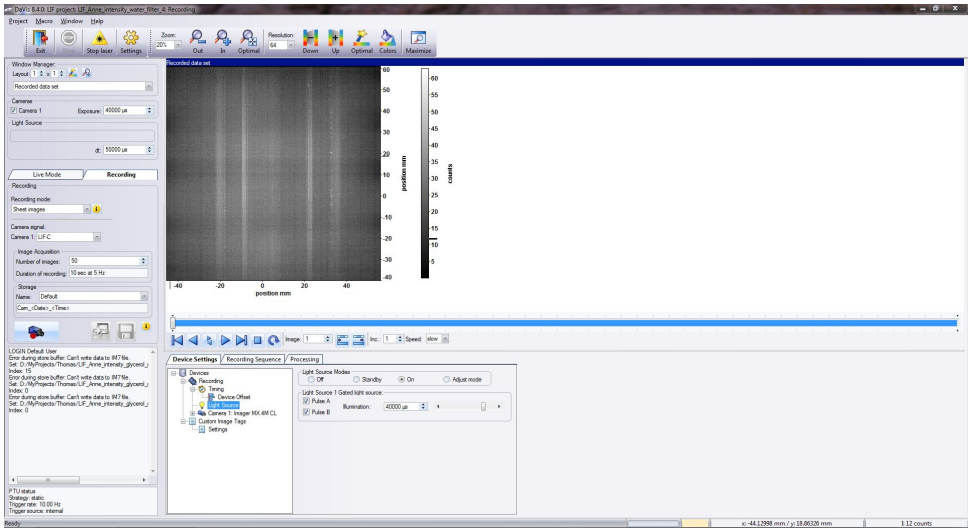

Figure A.5

Again, click "Exit" and select the sheet image. Go to "Processing", see figure. Right-click 2. and select "Background subtraction" from "LIF". Right-click 3. and select "Sheet processing" from "LIF". Click "Start Processing". The sheet image will now be processed.

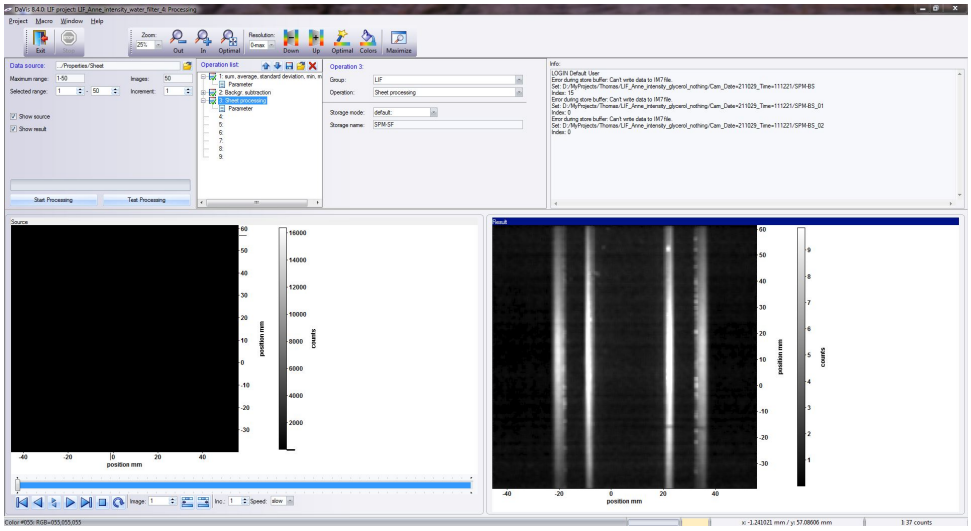

Figure A.6

A.1.4. Concentration calibration

Go again to "Recording", and select "C-Calibration images" from the dropdown menu, see figure A.7. The calibration step is the most important and time consuming step. It is important because the predetermined particle concentration is related to the measured intensity that the fluorescent particles emit as a result of the excitation by the laser light. It is time consuming because essentially the same process is repeated six times. Number of images is still 50. Click the recording button. This is the 0 % concentration image, rename it to C-Calibration0. Now add particle solution, say 200 μL, bubble for around half a minute and let rest until no bubbles are present anymore. Repeat the recording step. This is the 20% concentration image. Repeat for 40%, 60%, 80% and 100%.

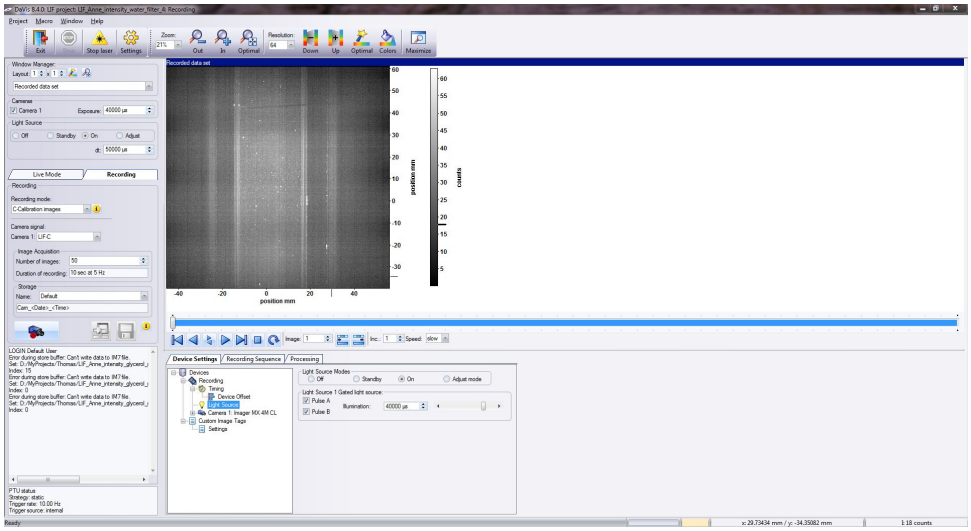

Figure A.7

Click "Exit" and select the 100 % image. Go to "Concentration" in the top bar, see figure A.1. Go to "Define Mask" in the top bar, see figure A.8. In this menu, select the part of the bubble column that you want to base your measurement on, the mask. When clicking "Exit", a popup will appear. Click "Save mask" and return to the project main page.

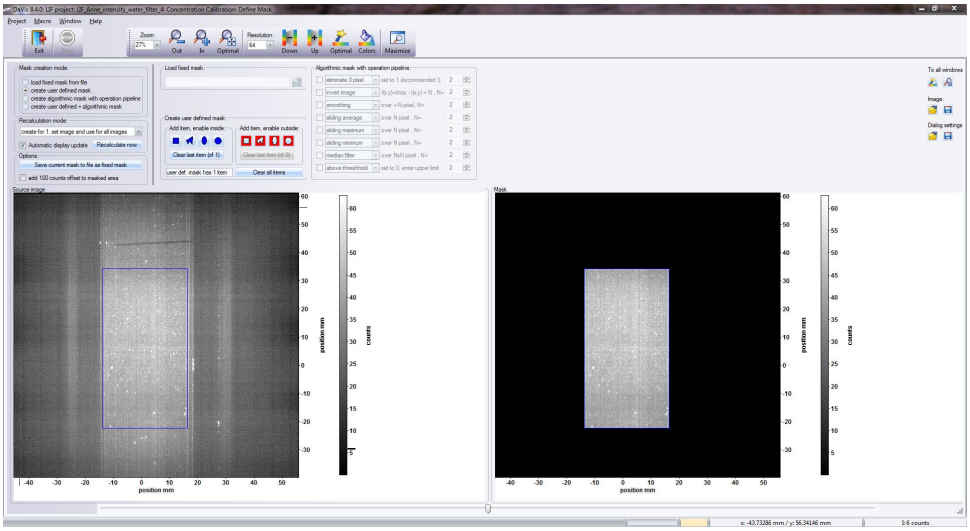

Figure A.8

Now select the 0% image and click "Processing". Set 3. to "Sheet correction" from "LIF", 4. to "Image correction (raw to world)" from "Image mapping" and 5. to "Apply mask" from "masking functions", see figure A.9. Click "Start Processing". Repeat for the other concentration images.

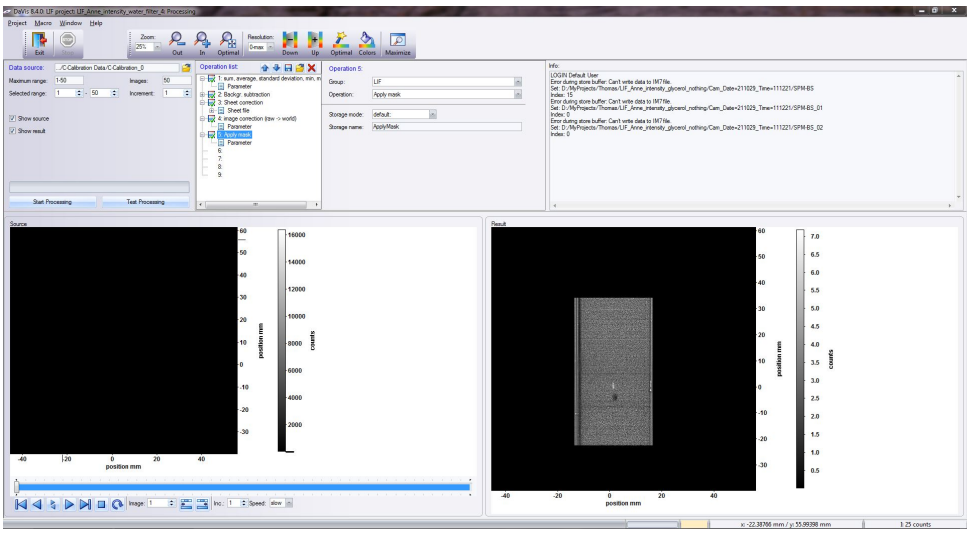

Figure A.9

Now return to the project main menu. In the 0% image, click all the plusses until you reach "Apply mask", see figure A.10.

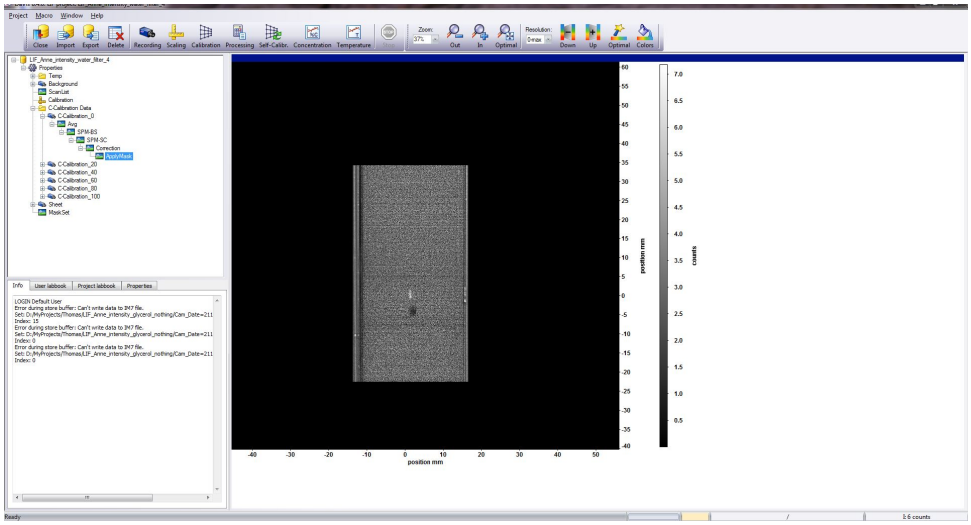

Figure A.10

Select "Apply mask" and click "Concentration" in the top bar. This will take you to the concentration menu, see figure A.11. In the left column is the intensity count of the image and its uncertainty and allotted concentration. Adjust the concentration and click "Add current parameter to sample list". The concentration, count and uncertainty will appear in the right column, as well as in the graph in the lower middle. Click "Save calibration". If a popup appears and says "Concentration Calibration already exists!", click "Overwrite". Exit and repeat for the other concentration images. You now have a working calibration curve! DaVis always sets the offset to 0, so the calibration curve will never fit perfectly as the count at 0 % is never actually 0.

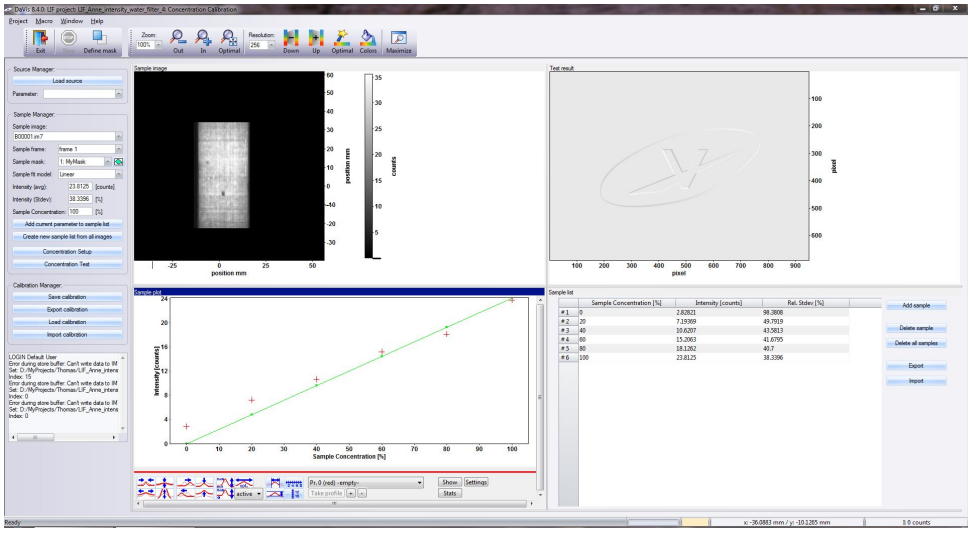

Figure A.11

A.1.5. Experiment

Now, finally, it is time for the actual experiment images. To take them, go to "Recording" and select "Experiment images" in the dropdown menu. Press the record button. Once your 50 images are taken, go to processing. Right-click 1. and select "Disable operation". This will generate 50 separate images instead of an average. Set 6. to "Concentration Calculation" from "LIF" and 7. to "x-y plot" from "profiles and time plots", see figure A.12. Press "Start Processing". This may take around two minutes.

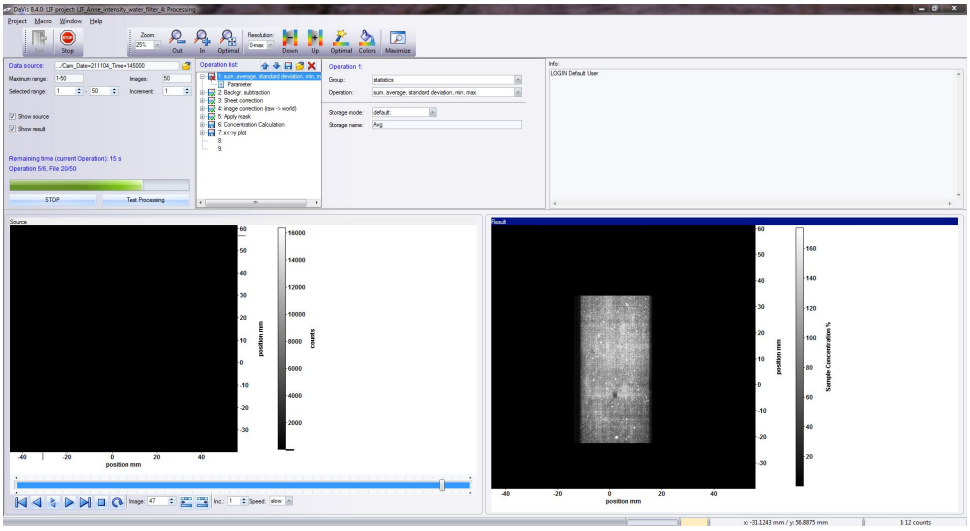

Figure A.12

When it is done, exit the processing menu and click all the plusses until you reach the x-y plot, see figure A.13. This is your data, every image taken by the camera has been averaged into a point.

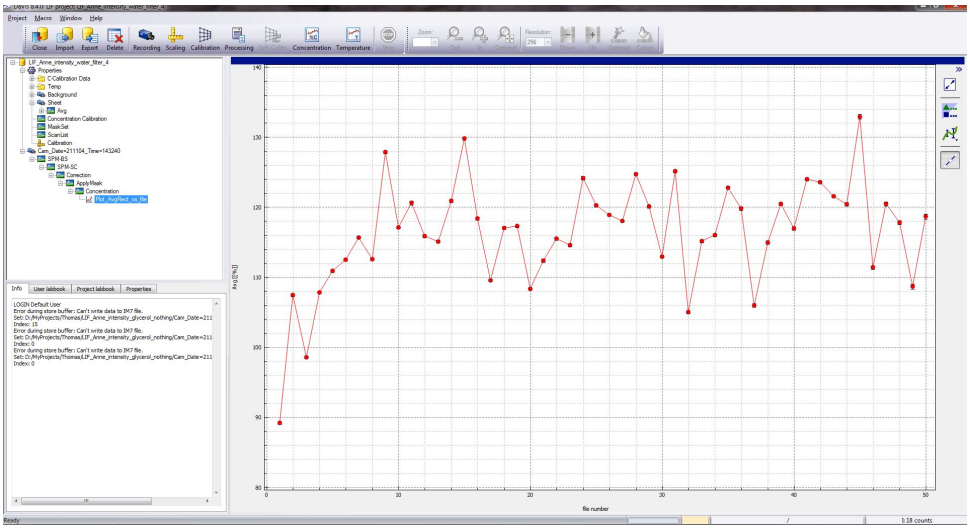

Figure A.13

To export the data for further processing, in the top bar, click "Export". This is the export menu, see figure A.14. Export the plot as a picture, or the data points in number values. To export the data to a text file, select ASCIItext(txt). Select a map on the desktop to export it to and click "Export".

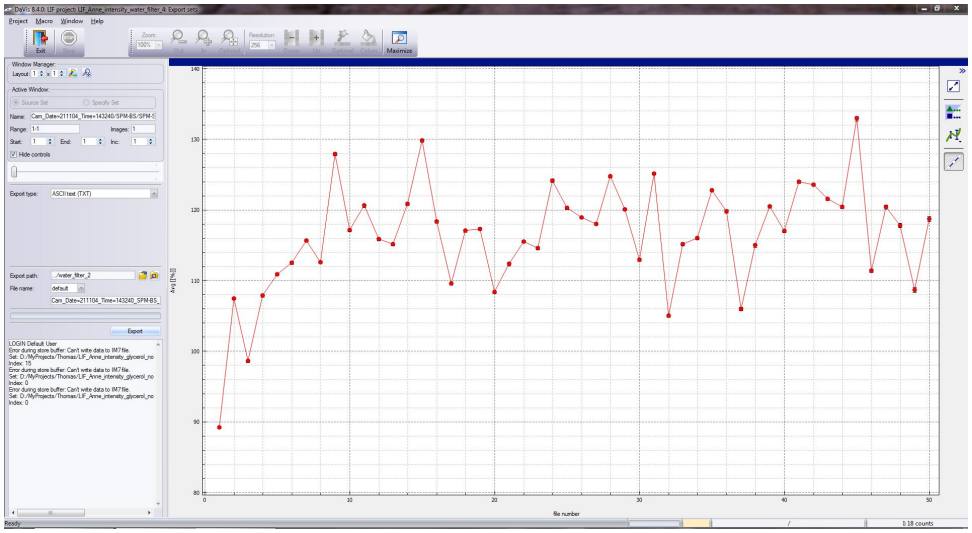

Figure A.14

Your data will be stored in a textfile, which looks something like figure A.15. This data can be further processed if needed.

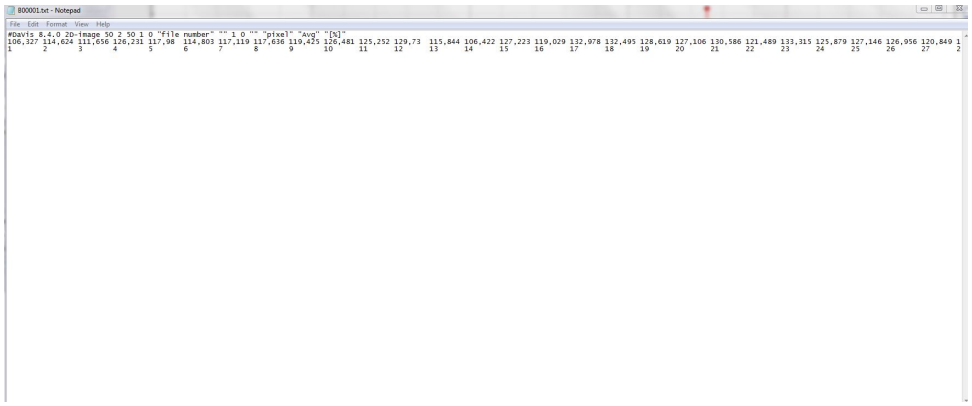

Figure A.15

The exporting of the data concludes this section on image processsing.

A.2. Bubble correction and plotting sequence

In this section, the bubble correction process is detailed. First, a short derivation for equation 3.4.1 is given. Then, the Python script for determining the calibration curves is provided in A.2.1. The raw data points to plot have been removed, the corresponding figures are figures 4.2 to 4.5. A table with all slopes and offsets for the calibration curves is also present, as well as the method for calculating the error in flow rate. Next, the method for processing the raw data is presented. Lastly, the correction and plotting sequence for the concentration measurements is given. The plots generated by this sequence are figures 4.6 to 4.10.

A.2.1. Bubble correction calibration curves

Graphic derivation of equation 3.4.1

A short graphic derivation of equation 3.4.1 is given here. The curve is the expected course of a measurement sample of a pre-determined concentration. A measurement point obtained during a bubbling measurement can lie both above and below this curve at the same x-postion, namely the same flow rate, see figure **??**.

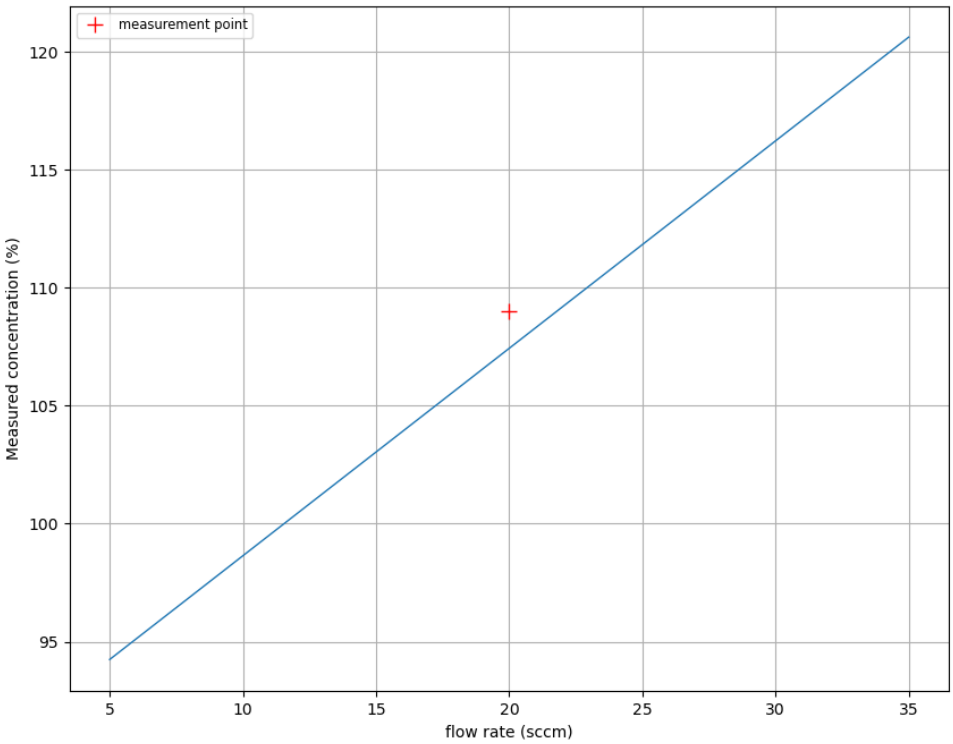

Figure A.16: Example of a linear bubble correction curve with an example measurement point at 14 sccm.

Equation 3.4.1 scales the curve such that it is a horizontal line at the pre-determined concentration, and scales the measurement point with it.
First, the scaling factor $\frac{1}{a*\text{flow rate}+b}$ reduces the linear curve to a horizontal line at unity, and the point is scaled also in the same way. This can be seen in figure A.17.

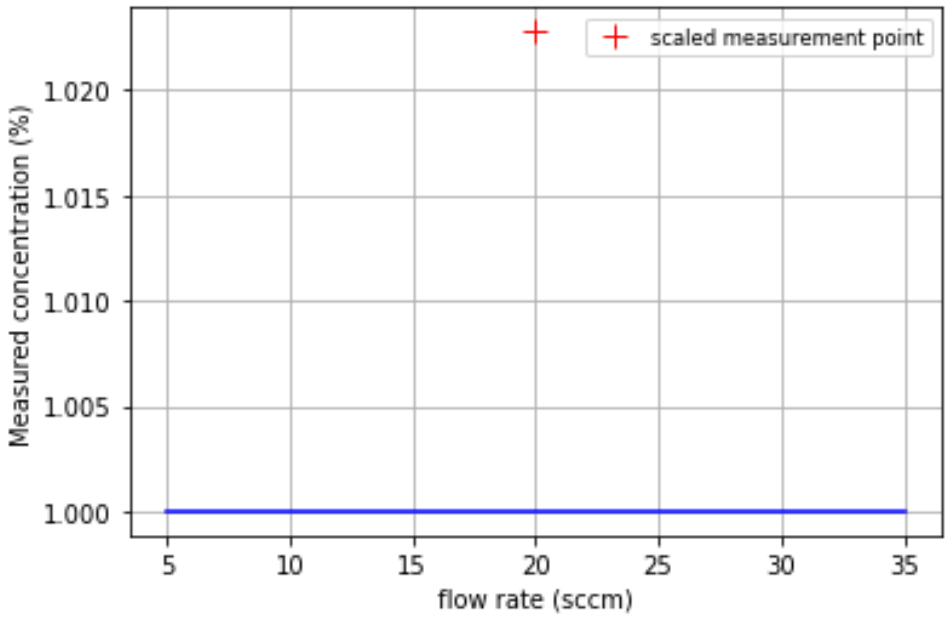

Figure A.17: The linear bubble correction curve has been scaled to be a line at unity, and the measurement point is scaled in the same way.

Then, the horizontal line is multiplied with the pre-determined concentration that was present at the beginning of the bubbling experiment, say 100%. The measurement point has also been multiplied by this pre-determined

concentration value, and is now corrected for bubbling. This can be seen in figure A.18.

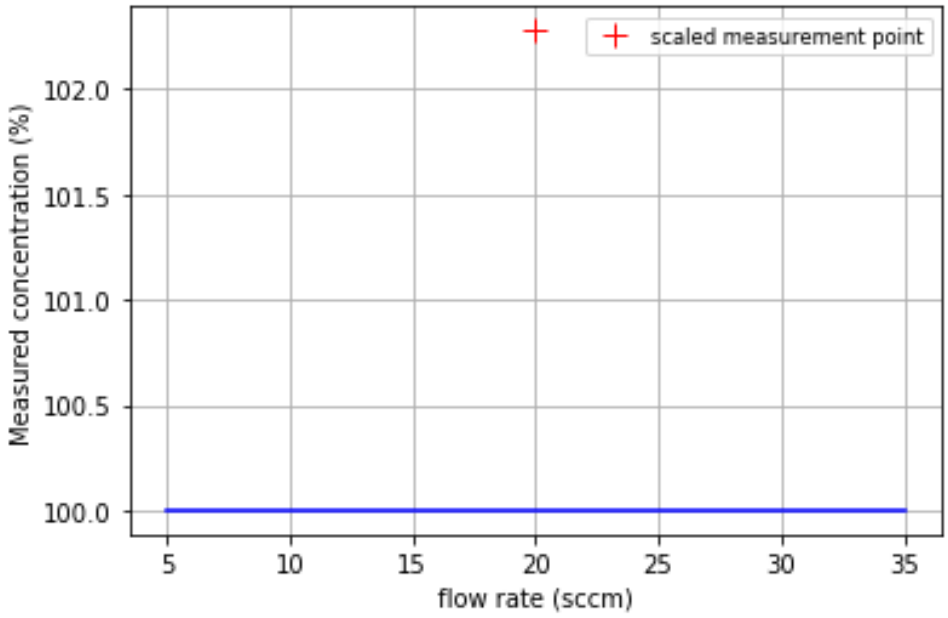

Figure A.18: The horizontal line at unity has been multiplied with the pre-determined concentration, 100%, and the measurement point is now corrected for bubbling.

Bubble calibration curves plotting sequence

```
    #script for plotting bubbling calibration data points
# fits a calibration curve through the data points and plots it
#returns fit parameters

#import numpy, import matplotlib, import scipy
import numpy as np
import matplotlib.pyplot as plt
from scipy import optimize

#function for fitting data along expected linear relationship a*x+b
#prints the fit parameters a and b
#plots the fitted function
def fit_plot(flow_rate,conc):
    def fit_func(x, a, b):
        return a*x+b

    params, params_covariance = optimize.curve_fit(fit_func, flow_rate,conc,
                                                   p0=[2, 2])
    print(params)
    print(np.sqrt(np.diag(params_covariance))
    plt.plot(flow_rate,fit_func(flow_rate,params[0],params[1]),linewidth=1)

#define plotting sequence
#plot for 6 different expected concentrations
#define simulant fluid to print
def plot(flow_rate,conc0,conc20,conc40,conc60,conc80,conc100,fluid, size):
        plt.figure(figsize=(10, 8), dpi=100)
        #plot measured concentration vs flow rate for all 6 expected concentrations
        #plot with plusses at measurement points
        plt.plot(flow_rate,conc0,'+',markersize=10,label="0% concentration")
```

```
        plt.plot(flow_rate,conc20,'+',markersize=10,label="20% concentration")
        plt.plot(flow_rate,conc40,'+',markersize=10,label="40% concentration")
        plt.plot(flow_rate,conc60,'+',markersize=10,label="60% concentration")
        plt.plot(flow_rate,conc80,'+',markersize=10,label="80% concentration")
        plt.plot(flow_rate,conc100,'+',markersize=10,label="100% concentration")
        #fit data and plot fitted curve
        print(fluid)
        fit_plot(flow_rate,conc0)
        fit_plot(flow_rate,conc20)
        fit_plot(flow_rate,conc40)
        fit_plot(flow_rate,conc60)
        fit_plot(flow_rate,conc80)
        fit_plot(flow_rate,conc100)
        #figure formatting
        plt.xlabel("flow rate (sccm)")
        plt.ylabel("Measured concentration (%)")
        plt.grid()
        plt.legend(fontsize='small')
        plt.show()

#define flow_rate array from 5 to 35 in increments of 5
flow_rate=np.linspace(5,35,7)

#define flow_rate_glycerol array from 0 to 16 in increments of 2
flow_rate_glycerol=np.linspace(6,16,6)

#measurement arrays water

#measurement arrays 41.6% wt glycerol for flow rates 0 to 16


#plot for water
plot()
#plot for 41.6 % wt glycerol for flow rates 0 to 16
plot()
```

The fitting of the data points results in the slopes and offsets is presented in the following table:

Table A.1: Slopes and offsets of bubbling calibration curves for water and aqueous 41.6 % glycerol for several pre-determined concentrations.

Pre-determined concentration	Slope water	Offset water	Slope 41.6 % wt glycerol	Offset 41.6 % wt glycerol
0%	0.14	8	2.96	25
20%	0.28	20	4.4	66
40%	0.57	35	5.1	95
60%	0.54	59	5.94	120
80%	0.72	75	7.14	134
100%	0.88	90	8.59	150

A.2.2. Mass flow controller error

The percentual error in the mass flow controller is calculated using the following Python script:

```
#import numpy
    import numpy as np

#function for calculating height in column to volume
#height times surface area, 25.7 mm being the column diameter and 27 being the column de
# times 1e-3 to get mL
```

```
def volume(h):
    volume= (25.7**2*np.pi/4*(h+27))*1e-3
    return volume

#function for taking standarddeviation, mean and error of measurement array
#print error, fluid and sccm
def var_holdup(holdup,fluid,sccm):
    mean=np.mean(holdup)
    std=np.std(holdup)
    error=std/mean*100
    print("The error for gas holdup in "+ fluid+ " for a flow rate of "+sccm+" sccm is "

h_6_glycerol=np.array([])
h_8_glycerol=np.array([])
var_holdup(holdup_6_glycerol, "41.6% wt glycerol", "6")
var_holdup(holdup_8_glycerol, "41.6% wt glycerol", "8")
```

A.2.3. Values and errors of the measurements

As noted before, a measurement point consists of 50 images, of which about 35 to 40 are useful. The concentration values of these points are processed using the following Python script.

```
    #script to condense the 50 images of a measurement to 1 data point with error
#import numpy
import numpy as np

#function that returns the mean and standarddeviation and puts them in lists
#the mean has no decimals, the standarddeviation 1 decimal
def values(values):
    mean.append(np.around(np.mean(values)))
    std.append(np.around(np.std(values),1))

#define the empty lists to put the mean and standarddeviation values in
mean=[]
std=[]
#data arrays for every timepoint
water_hall_2_min5=np.array([])
values(water_hall_2_min5)
water_hall_2_0=np.array([])
values(water_hall_2_0)
water_hall_2_5=np.array([])
values(water_hall_2_5)
water_hall_2_10=np.array([])
values(water_hall_2_10)
water_hall_2_15=np.array([])
values(water_hall_2_15)
water_hall_2_20=np.array([])
values(water_hall_2_20)
water_hall_2_25=np.array([])
values(water_hall_2_25)
water_hall_2_30=np.array([])
values(water_hall_2_30)
water_hall_2_35=np.array([])
values(water_hall_2_35)
#print mean and standarddeviation lists
print(mean)
```

```
print(std)
```

A.2.4. Correction and plotting sequence

The combined correction and plotting sequence for the particle extraction measurements. Note that the errors for the data points while bubbling are larger because of the error correction.

```
#script to correct the particle extraction measurement data and plot it

#import numpy, matplotlib
import numpy as np
import matplotlib.pyplot as plt

#define plotting sequence
def plot(time,conc_water,conc_glycerol,method,yerr_water,yerr_glycerol,xerr):
        plt.figure( dpi=120)
        #plot measured concentration vs flow rate for all 6 expected concentrations
        #plot with errorbars
        plt.errorbar(time,conc_water,yerr_water,xerr,label="water")
        plt.errorbar(time,conc_glycerol,yerr_glycerol,xerr,label="41.6% wt glycerol")
        #figure formatting
        plt.xlabel("time (min)")
        plt.ylabel("Measured concentration (%)")
        plt.grid()
        plt.legend(fontsize='medium')

#define correction step for bubbling
#correct error arrays because the bubbling correction influences the error
def calibration(arr_bubbling,arr_start,arr_end,coeff,offset,coeff_error,
                offset_error,yerr,sccm):
    #first do the bubble correction
    factor=(sccm*coeff+offset)/100
    arr_cal=arr_bubbling/factor
    #then do the error correction
    yerr_min5=np.array(yerr[:1])
    yerr_35=np.array(yerr[-1:])
    yerr_middle=yerr[1:-1]
    #first determine the correction error by quadrature
    correction_error=np.sqrt(coeff_error**2+offset_error**2)
    #then correct the middle yerr array by quadrature by working
    in fractional errors
    dyerr=np.sqrt((correction_error/(coeff+offset))**2+
    (yerr_middle/arr_bubbling)**2)
    yerr=dyerr*arr_bubbling
    return np.concatenate((arr_start,arr_cal,arr_end)),
           np.concatenate((yerr_min5,yerr,yerr_35))



#define time array
t=np.linspace(-5,35,9)

#coefficient and offset for correction
coeff_water=0.87857143
coeff_glyc=8.58571429
offset_water=89
```

```
offset_glycerol=150

#flow rates
sccm_water=20
sccm_glycerol=12

#error in coefficient and offset
#taken from the covariance of the fit parameters
coeff_error_water=0.03
coeff_error_glycerol=0.42
offset_error_water=0.7
offset_error_glycerol=4.81

#measurement arrays

water_bubbling_filter=np.array([])
start_water_filter=np.array([])
end_water_filter=np.array([])

glycerol_bubbling_filter=np.array([])
start_glycerol_filter=np.array([])
end_glycerol_filter=np.array([])




#define errors
yerr_water_filter=np.array([])
yerr_glycerol_filter=np.array([])

#execute bubbling correction
#execute error correction
water_filter,yerr_water_filter=calibration()
glycerol_filter,yerr_glycerol_filter=calibration()

#execute plotting sequence
plot(t,water_filter,glycerol_filter,"filter",yerr_water_filter,
     yerr_glycerol_filter,xerr=None)
```